ABSTRACT

CHAPMAN, PETER HENRY. Exploiting Fission Chain Reaction Dynamics to Image Fissile Materials. (Under the direction of John Mattingly.)

Radiation imaging is one potential method to verify nuclear weapons dismantlement. The neutron coded aperture imager (NCAI), jointly developed by Oak Ridge National Laboratory (ORNL) and Sandia National Laboratories (SNL), is capable of imaging sources of fast (e.g., fission spectrum) neutrons using an array of organic scintillators. This work presents a method developed to discriminate between non-multiplying (i.e., non-fissile) neutron sources and multiplying (i.e., fissile) neutron sources using the NCAI. This method exploits the dynamics of fission chain-reactions; it applies time-correlated pulse-height (TCPH) analysis to identify neutrons in fission chain reactions. TCPH analyzes the neutron energy deposited in the organic scintillator vs. the apparent neutron time-of-flight. Energy deposition is estimated from light output, and time-of-flight is estimated from the time between the neutron interaction and the immediately preceding gamma interaction. Neutrons that deposit more energy than can be accounted for by their apparent time-of-flight are identified as fission chain-reaction neutrons, and the image is reconstructed using only these neutron detection events. This analysis was applied to measurements of weapons-grade plutonium (WGPu) metal and ^{252}Cf performed at the Nevada National Security Site (NNSS) Device Assembly Facility (DAF) in July 2015. The results demonstrate it is possible to eliminate the non-fissile ^{252}Cf source from the image while preserving the fissile WGPu source. TCPH analysis was also applied to additional scenes in which the WGPu and ^{252}Cf sources were measured individually. The results of these separate measurements further demonstrate the ability to remove the non-fissile ^{252}Cf source and retain the fissile WGPu source. Simulations performed using MCNPX-PoliMi indicate that in a one hour measurement, solid spheres of WGPu are retained at a 1σ level for neutron multiplications $M \simeq 3.0$ and above, while hollow WGPu spheres are retained for $M \simeq 2.7$ and above.

Exploiting Fission Chain Reaction Dynamics to Image Fissile Materials

by
Peter Henry Chapman

A dissertation submitted to the Graduate Faculty of
North Carolina State University
in partial fulfillment of the
requirements for the Degree of
Doctor of Philosophy

Nuclear Engineering

Raleigh, North Carolina

2017

APPROVED BY:

Joseph Doster	David Lalush

Paul Hausladen	John Mattingly
	Chair of Advisory Committee

BIOGRAPHY

Pete Chapman earned a Bachelor of Science degree in Engineering Physics at the United States Military Academy and was commissioned into the Army as an infantry officer in 1998. He earned a Master of Science degree in Nuclear Science and Engineering at the Massachusetts Institute of Technology and joined the faculty of the Department of Physics and Nuclear Engineering at the United States Military Academy in 2010. Pete was promoted to his current rank of Lieutenant Colonel in 2014 and will rejoin the faculty at the United States Military Academy upon the successful completion of his Ph.D.

ACKNOWLEDGEMENTS

TABLE OF CONTENTS

LIST OF TABLES

LIST OF FIGURES

CHAPTER

1

INTRODUCTION

Nuclear weapon states that are signatories to the Treaty on the Non-Proliferation of Nuclear Weapons (NPT) are legally bound to disarm [49]. Since the NPT entered into force in 1970, strides have been made toward that goal; however, there are an estimated 14,000 nuclear warheads in the US and Russian stockpiles alone [23]. The current nuclear arms control agreement between the US and Russia is the New Strategic Arms Reduction Treaty (New START), which went into force in 2011 and whose limits on strategic arms are to be met in 2018 for a duration of ten years [36] [54]. This treaty classifies each deployed strategic bomber or re-entry vehicle on a ballistic missile as one warhead [43].

In the event that there are new arms control agreements in the future and further reductions in nuclear stockpiles, it will be necessary to count and verify individual warheads because the

relative importance of a single warhead will increase in a breakout scenario[1] [12]. The verification of individual warheads is challenging because the observer desires certainty that a warhead declared by the host is actually a warhead, while the host cannot reveal any classified weapon design information.

One verification methodology is to perform measurements on a device proffered as a warhead to confirm a series of attributes. Each attribute[2] definitively indicates whether the device could be, or is definitely not, a nuclear warhead [53] [12]. The intent of this approach is that a candidate with a sufficient amount of "could be" classifications would be identified as a warhead with a degree of certainty acceptable to an observer without revealing classified device characteristics. This approach, referred to as an attribute measurement system, is nuclear verification in the form of the "20 questions" game a child (observer) plays to determine what someone else (host) is thinking of (if a device to be verified is indeed an actual warhead) in a series of questions with binary answers that gradually reveal information until a conclusion is reached.

Neutron multiplication, the ability to sustain a fission chain reaction, is a suitable attribute for this methodology. Because a nuclear warhead, by definition, must be able to sustain a fission chain reaction, the ability to classify a device as non-multiplying would identify that candidate as a spoof to an observer. Incorporating this classification in an imaging system of suitable resolution would allow the verification of multiple sources grouped together, e.g., multiple warheads on the bus of a missile, and provide information about the geometry of the source.

The purpose of this work is to develop a methodology that classifies a neutron source as a multiplying assembly (or not) in a scene that may contain inhomogeneous, extended, or multiple sources. It is not intended to be a complete solution to warhead verification challenges by itself, but rather answers two of the "20 questions" (neutron multiplication and source geometry) as part of a larger verification methodology that meets the needs of both observer and host.

---

[1]A breakout scenario is when a state secretly obtains or maintains more nuclear weapons than it has previously declared.

[2]An example attribute is the presence of highly enriched uranium or weapons grade plutonium. A device having this attribute could possibly be, but is not necessarily, a nuclear warhead. Conversely, the absence of highly enriched uranium or weapons grade plutonium indicates a device is definitely not a nuclear warhead.

2

1.1 Previous Work

The previous work considered in the preparation of this dissertation falls into three broad categories: technical measures for warhead verification, identifying multiplying assemblies, and imaging neutron sources. The following is a brief synopsis of each of these areas.

1.1.1 Technical Measures for Warhead Verification

Traditional technical means for warhead verification involve measurement of the gamma and neutron signatures unique to highly enriched uranium (HEU) or weapons grade plutonium (WGPu). The measurements of special nuclear material (SNM) are either active or passive, where active measurements use an external source of ionizing radiation to induce the signature of interest.

1.1.1.1 Highly Enriched Uranium

The passive neutron signature from HEU is vanishingly small because its spontaneous fission yield is on the order of 10^{-4} neutrons per second per gram. Passive gamma detection of HEU relies heavily on the 186 keV line from ^{235}U, which may be used to estimate the enrichment of a sample. However, this gamma emission is shielded relatively easily and has a mean free path in HEU metal of 0.4 mm [44]. The absence of strong passive signatures may be overcome by active measurements of HEU.

Active interrogation methods typically rely on gammas and neutrons emitted following the beta decay of fission products [47]; these emissions are referred to as beta-delayed particles. In these techniques, a pulsed gamma or neutron source is used to induce fissions in an inspected object. The beta-delayed signatures are then measured between source pulses. Analysis of beta-delayed neutrons is discussed in the next section.

The highest energy background gamma line, due to the decay of ^{232}Th, is 2.6 MeV. Beta-delayed gammas can have more than double this energy, so the detection of gamma radiation above 2.6 MeV

3

suggests the presence of SNM. This method has been incorporated into a system designed to identify the presence of SNM in cargo. In this system, gamma emissions between 2.5-6.0 MeV were used to detect SNM assemblies as small as 5 kg [15] [47].

1.1.1.2 Weapons Grade Plutonium

In contrast to HEU, the neutron and gamma signatures for WGPu can be measured passively. The spontaneous fission neutron production rate for WGPu metal is on the order of 100 neutrons per second per gram, more than six orders of magnitude greater than HEU [44]. A neutron multiplicity counting measurement may be performed to estimate the mass of plutonium, neutron multiplication, and confirm the absence of plutonium oxide in a sample [1]. The technique of neutron multiplicity counting is described in the next section.

The passive gamma signature of WGPu relies on three groups of lines. A gamma spectrum of WGPu measured by a 150% efficient[3] high purity germanium detector, is shown in Figure 1.1. The first group of lines falls between 330-350 keV and may be used to estimate the time since the last ^{241}Am chemical separation [26]. The peaks in this region, highlighted in red in Figure 1.1(a) and shown in Figure 1.1(b), are due to the decay of ^{239}Pu, ^{237}U, and ^{241}Am. The second group of lines falls between 630-670 keV and may be used to estimate the ^{240}Pu/^{239}Pu isotopic ratio [26]. The peaks in this region, highlighted in green in Figure 1.1(a) and shown in Figure 1.1(c), are due to the decay of ^{239}Pu, ^{240}Pu, and ^{241}Am. The last line at 870.7 keV is due to the de-excitation of the first excited state of ^{17}O [55]. Oxide presence in the plutonium sample is confirmed if this peak is present. These analysis methods are collectively referred to as the Pu-300, Pu-600, and Pu-900 techniques [26].

---

[3]High purity germanium detectors are characterized by their efficiency relative to a 3 in × 3 in NaI(Tl) detector [13].
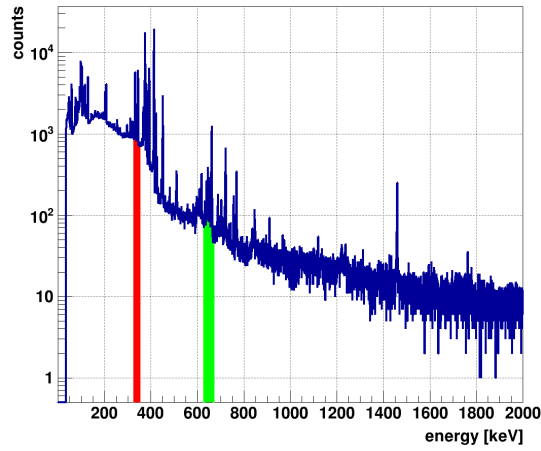
(a)
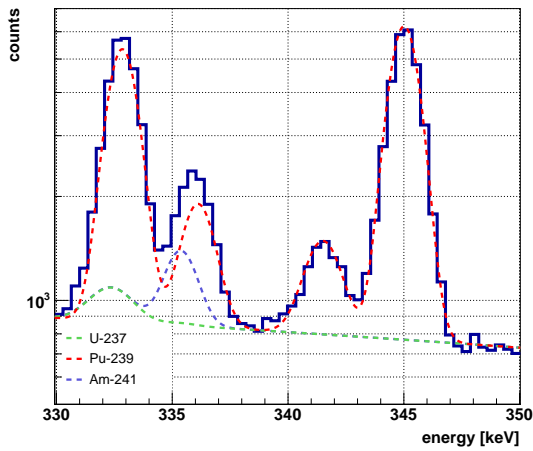
(b)
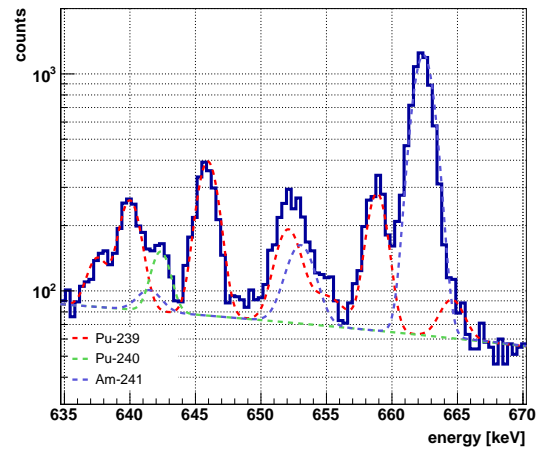
(c)

Figure 1.1 Pu-300 and Pu-600 regions of interest. The (a) gamma spectrum of weapons grade plutonium is shown with the (red) Pu-300 and (green) Pu-600 regions highlighted. The (b) 330-350 keV region is used to estimate the time since the last ^{241}Am chemical separation. The (c) 630-670 keV region is used to estimate the ^{240}Pu/^{239}Pu isotopic ratio.

In general, gamma signatures from SNM are used to estimate the isotopic composition of a sample because their energies are characteristic of the source isotopes. These gammas have mean free paths on the order of less than a centimeter in SNM metal, so they provide information

5

only about the surface materials of an inspected weapon. The spontaneous or induced neutron signatures of SNM are used to identify a source as multiplying, and in some cases, estimate its multiplication. Neutrons penetrate SNM more readily than gammas; using neutrons to identify multiplying assemblies is discussed next.

1.1.2 Identifying Multiplying Assemblies

Nuclei that split when struck by a neutron are fissionable, and nuclei that undergo this reaction for neutrons of any incident energy are fissile [25]. An arrangement of fissile material capable of supporting a fission chain reaction is a multiplying assembly[4]. Three methods of identifying multiplying assemblies are discussed in this section: neutron multiplicity counting, pulsed neutron interrogation, and time-correlated pulse-height analysis.

1.1.2.1 Neutron Multiplicity Counting

Neutron multiplicity counting is a technique that may be used to estimate the ^{240}Pu mass, neutron multiplication, and (α, n) reaction rate of a source as a function of the first three moments of an observed neutron multiplicity distribution [9]. The neutron multiplicity distribution is the probability distribution of the number of neutrons observed in coincidence. This method grew from neutron coincidence counting measurements by including the observation of the distribution's third moment as a third observable in the 1980s, thereby enabling the addition of a third parameter for which to solve [45] [6]. Material assay precision of under 10% for plutonium samples measured for under one hour are typical [9].

A multiplicity measurement is conducted by recording the time of neutron detection inside a group of detectors. Typically, these measurements are performed with moderated ^{3}He proportional counters; however, the use of organic scintillators is the subject of recent research [35] [8]. The

---

[4]A fission chain reaction is a series of reactions whereby a neutron born in the fission of one nucleus induces fission in another nucleus. Fission chain reactions are described in further detail in Chapter 2.

recorded pulse train is then analyzed by the application of a fixed coincidence gate width along its length to create a histogram of the number of events observed in coincidence. An example pulse train from a neutron multiplicity measurement is shown in Figure 1.2. The histogram forms the multiplicity distribution whose moments are then related to the parameters of interest. An example distribution from the measurement of a 4.5 kg WGPu sphere surrounded by a 1.5 in polyethylene shell is shown in Figure 1.3 [29]. This experiment used a coincidence gate width of 1024 μs.
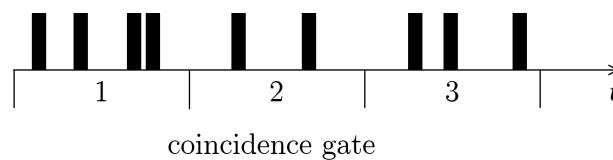
Figure 1.2 Example pulse train from a neutron multiplicity experiment. The vertical blocks represent the detection of a neutron along the horizontal time axis. The counts observed within each coincidence gate are used to create a histogram of the neutron multiplicity distribution.
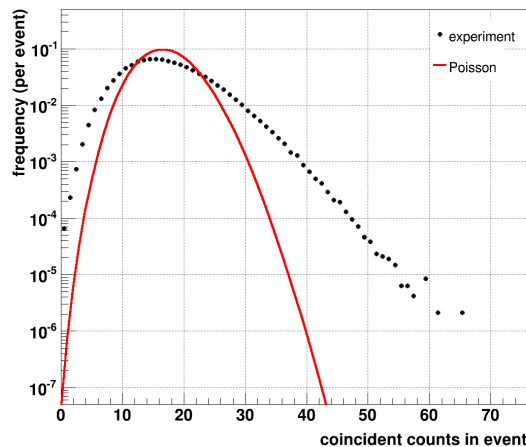
Figure 1.3 Neutron multiplicity distribution for a 4.5 kg WGPu sphere surrounded by a 1.5 in polyethylene shell. The (black dots) measured neutron multiplicity distribution is shown compared to a (red line) Poisson distribution with the same mean. The distribution shown used a coincidence gate width of 1024 μs [29].

7

For a source where each neutron emission is independent, such as one based on an (α, n) reaction, the neutron multiplicity distribution is a Poisson distribution because each detected event is independent of all other events. On the other hand, detected events from spontaneous fission sources may be correlated, i.e., multiple neutrons from the same fission event may be detected in coincidence. The distribution from a spontaneous fission source will therefore deviate from a Poisson distribution and exhibit a larger variance. Neutron multiplicity distributions of multiplying sources exhibit still larger variances because multiple generations in a fission chain reaction are correlated, and multiple neutrons from the same fission event or from different generations in a fission chain reaction may be detected in coincidence. Figure 1.3 shows the multiplicity distribution of a multiplying assembly compared to a Poisson distribution with the same mean.

The relationships between the observed quantities (the moments) and estimated parameters (^{240}Pu mass, neutron multiplication, and (α, n) reaction rate) are derived using two key assumptions [9]. First, all induced fission neutrons are assumed to be emitted at the same time as the source neutron; this concept is called super-fission. Second, the probabilities of fission and detection are assumed to be constant over the source volume. These assumptions effectively remove the time and spatial dependence of fission chain reactions from the analysis.

1.1.2.2 Pulsed Neutron Interrogation

Delayed neutrons are those emitted following the beta decay of fission products. The detection of delayed neutrons is therefore indicative of fissionable material. As their name suggests, these neutrons are born late relative to the fission event that created their precursors. Approximately 270 precursors emit delayed neutrons; these precursors decay with half-lives between hundreds of milliseconds to tens of seconds, whereas prompt fission neutrons are emitted on a femtosecond time scale [47]. Delayed neutron yields are less than 1% of prompt neutron yields, and are therefore difficult to observe in a passive measurement [44].

However, the temporal distribution of delayed neutrons may be observed in an active measure-

ment using a pulsed source to induce fission in an inspected object. Typical pulsed sources include DT (deuterium-tritium) neutron generators or bremsstrahlung X-ray generators using electron linear accelerators [47]. A measurement is conducted by inducing fission in the inspected object during the duty cycle of the pulsed source, thereby creating the precursors to beta decay. The time of neutron events is recorded between pulses; the presence of beta-delayed neutrons above background indicate the inspection object is fissionable. The recorded pulse train may then be analyzed as in a multiplicity measurement to estimate source multiplication, as demonstrated in [20].

Alternatively, energy sensitive detectors with a threshold of 1 MeV may be used to identify prompt neutrons between pulses. These neutrons are observable between pulses when a delayed neutron induces fission in a fissile material. The average delayed neutron energy is about 0.5 MeV, while the average prompt neutron energy is approximately 2 MeV [47]. Lower energy delayed neutrons induce fission only in fissile materials, as shown in a comparison of the ^{235}U (fissile) and ^{238}U (non-fissile) fission cross sections in Figure 1.4(a). This technique has been used to differentiate between HEU and depleted uranium [19].

The time distribution of prompt neutrons due to beta-delayed neutron induced fission in HEU metal is shown in Figure 1.4(b). The plot shows a one hour measurement of approximately 14 kg of HEU. The measurement was performed with a neutron energy deposition threshold of 1 MeV using the neutron coded aperture imager; this measurement system is described in detail in Section 2.7. Fissions in the HEU were induced by a DT generator operating at 300 Hz with a 10% duty cycle and time Δt is measured relative to the start of the DT generator pulse. The data acquisition system operated with a veto while the DT generator was on; no events were recorded in the interval $(0 < \Delta t < 333)$ ns. The die-away interval $(333 < \Delta t < 1500)$ ns shows the time scale in which the incident neutrons were moderated and induced fission in the HEU. The delayed interval $(1500 < \Delta t < 3000)$ ns shows where beta-delayed neutrons induced fission in the HEU. Because the passive neutron signature of the HEU is negligible, the observation of prompt neutrons in the delayed region indicates fissile material is present.

9
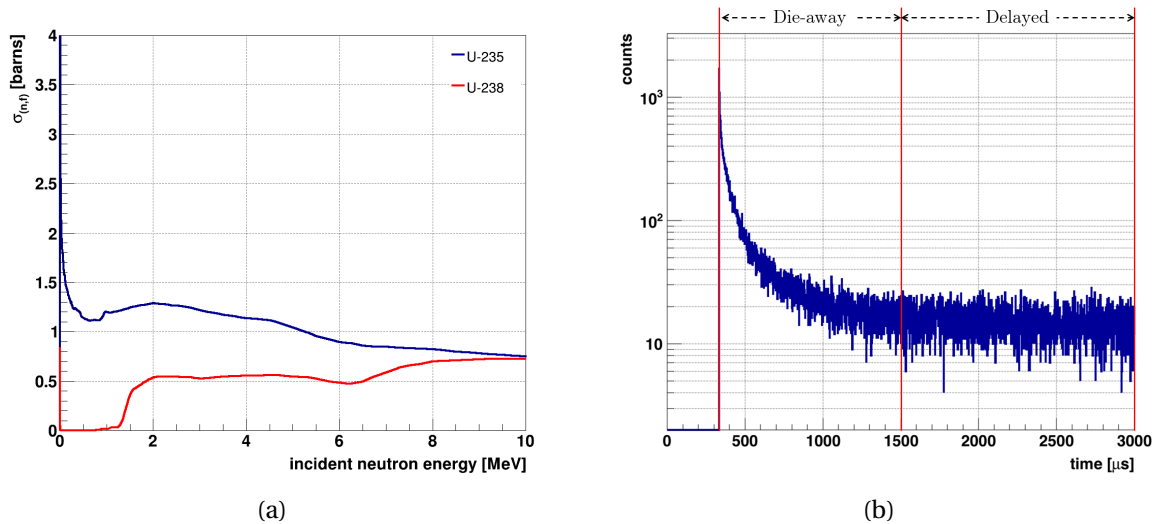
Figure 1.4 Detecting beta-delayed neutron induced fission. (a) The microscopic neutron induced fission cross sections $\sigma_{(n,f)}$ for (blue) ^{235}U and (red) ^{238}U are shown. The sharp drop off in the cross section for ^{238}U at about 1.5 MeV makes beta-delayed neutron induced fission in ^{238}U highly unlikely. (b) The active measurement of HEU shows the presence of prompt neutrons in the delayed region; these neutrons indicate the presence of a fissile material.

A spontaneous fission neutron source can also be used in place of an electronically pulsed source. These measurements use an intense ^{252}Cf source as the interrogation source. "Pulsing" of the ^{252}Cf is achieved by pneumatically moving the source between an interrogation position and a storage position shielded from the system's neutron detectors. Multiplying material may be identified by moderating the ^{252}Cf source such that the interrogating neutrons are below 1 MeV; Figure 1.4(a) shows non-fissile materials are insensitive to these energies [46].

1.1.3 Time-Correlated Pulse-Height Analysis

The time-correlated pulse-height[5] (TCPH) analysis technique is a means to identify a source as multiplying (or not) by comparing each neutron's apparent time-of-flight to the amount of en-

---

[5] Pulse-height in this context is a reference to the total energy deposited in a detector, as opposed to the detector's anode pulse amplitude.

ergy it deposits in a detector. The technique, first published in 2012, extends cross-correlation measurements by also considering energy as an observable parameter [31].

TCPH analysis is based on the assumption that a detected neutron is correlated to the gamma detected immediately preceding the neutron's arrival. The neutron time-of-flight is estimated from the time between the neutron interaction and the immediately preceding gamma interaction, while energy deposition is estimated from light output in an organic scintillator. Neutrons that deposit more energy than predicted by their apparent time-of-flight are identified as fission chain reaction neutrons; their presence indicates the source is multiplying. An example pulse height vs. apparent time-of-flight histogram from the measurement of WGPu metal is shown in Figure 1.5. The red line in this figure indicates where the energy deposited is equal to the kinetic energy predicted by the apparent time-of-flight. A more detailed explanation of TCPH analysis and the system used to acquire this measurement is presented in Chapter 2.
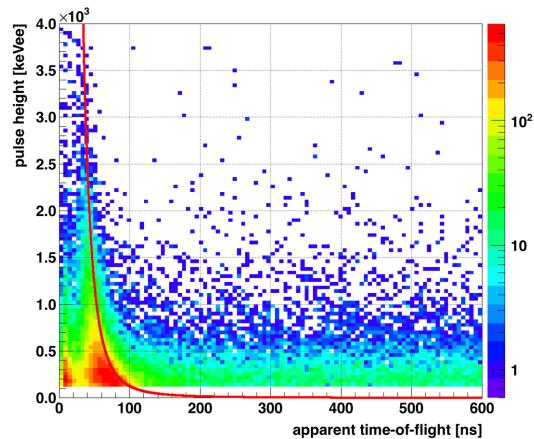
Figure 1.5 Example TCPH histogram from a WGPu measurement. The red line indicates where the energy deposited equals the kinetic energy predicted by the apparent time-of-flight. Events to the right of this line contain fission chain reaction neutrons.

11

The work presented in [31] performed passive measurements of low multiplication sources (mixed oxide (MOX) powder and plutonium-gallium disks) and MCNPX-PoliMi simulations of these measurements. This work, which was continued and published in [32], attempted to estimate source multiplication by analyzing the ratio of events with higher energy deposition than predicted by their time-of-flight to those with lower energy deposition.

The TCPH technique has also been employed in conjunction with active measurements of highly enriched uranium (HEU) in bare and reflected configurations [27, 40]. These measurements and corresponding simulations used a variety of neutron sources to interrogate HEU shells to estimate their neutron multiplication. Two additional series of passive measurements were performed independently at the Nevada Nuclear Security Site (NNSS) [33, 34]. These experimental campaigns measured the BeRP ball, a 4.5 kg sphere of weapons grade plutonium (WGPu) metal, in bare and reflected configurations. Both experiments were performed to estimate neutron multiplication.

Neutron multiplicity measurements have proven to be successful at estimating the multiplication of an inspected object. However, the assumptions necessary in the development of the technique are problematic in a scene involving inhomogeneous, extended, or multiple sources. TCPH analysis, on the other hand, imposes no constraints on the homogeneity of the source to be analyzed and requires only that multiple sources share the same source-detector distance.

1.1.4 Neutron Imaging

Radiation imaging enables the localization of nuclear material and increases the sensitivity of a measurement by allowing the directional rejection of background sources [28]. Neutron scatter cameras and coded aperture imagers are two alternative designs.

1.1.4.1 Neutron Scatter Cameras

A neutron scatter camera is typically composed of two planes of organic scintillators separated by a known distance. An example neutron scatter camera designed by the University of Michigan is shown

in Figure 1.6(a) [42]. An incident neutron that elastically scatters in both detector planes constitutes a measured event. The energy of the scattered neutron E_{n1} is estimated by the time-of-flight observed between the two planes. The energy deposited in the detector during the first scatter is added to E_{n1} to determine the incident neutron energy E_{n0}. The incident neutron direction is estimated by the kinematics of neutron-proton scattering; i.e., conservation of energy and momentum constrains the neutron source location to a conical surface for each measured event. A sketch of these interactions and a reconstructed cone are shown in Figure 1.6(b). The source image is formed by the intersection of many such cones projected onto a sphere surrounding the detector [28]. Typical neutron scatter cameras have angular resolutions between 12-20° [42] [28].

| (a) | (b) |
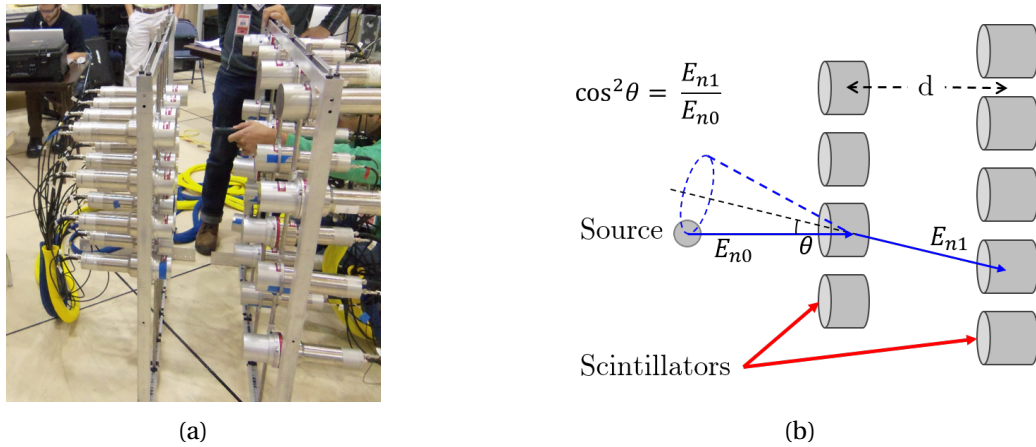
Figure 1.6 Neutron scatter camera. (a) A neutron scatter camera designed by the University of Michigan [42] and (b) a sketch illustrating the conical projection of a single measured event. Adopted from [16].

1.1.4.2 Coded Aperture Imagers

A coded aperture imager consists of a mask with an aperture pattern allowing the transmission of incident radiation and a position sensitive detector assembly. Incident radiation is spatially modulated by the aperture pattern on the mask, forming an encoded image in the detector. This image is

13

then decoded to create a reconstructed image of the source object [10] [3]. Fast neutron sources may be imaged by using a polyethylene mask and organic scintillator detectors; this technique will be discussed in more detail in Chapter 2. Coded aperture imagers are capable of less than 3° angular resolutions [18].

Neutron scatter cameras are capable of a 4π field of view; however, they have poor angular resolution and are less efficient relative to a coded aperture imagers. These characteristics make scatter cameras ideal for source localization. Coded aperture imagers have a limited field of view, but are capable of measurements with the resolution necessary to identify individual warheads on a single missile [18].

1.2   Original Contributions

There are two central elements to the purpose of this work: (1) classify a neutron source as multiplying (or not) and (2) perform this classification in a scene that may include inhomogeneous, extended, or multiple sources. Neutron multiplication was chosen as the attribute of interest because it is a necessary condition for a nuclear warhead, while other parameters such as isotopic composition and mass may be considered classified design characteristics. This work will consider an assembly of multiplying weapons grade plutonium.

This work describes a methodology to differentiate multiplying from non-multiplying assemblies in fast neutron images by incorporating time-correlated pulse-height analysis into the reconstruction of neutron coded aperture images. The combination of TCPH analysis and coded aperture imaging is a novel development and directly addresses a key limitation in the current state of the art: the ability to differentiate between multiplying and non-multiplying assemblies in a scene containing inhomogeneous, extended, or multiple inspection objects with the resolution necessary to distinctly identify each.

The methodology is experimentally demonstrated in three scenes involving weapons grade

14

plutonium (WGPu) and a (non-multiplying) ^{252}Cf point source, arranged separately and together. The effect of applying TCPH analysis is quantified, with uncertainty analysis, in each of the scenes. This work also employs computational modeling to estimate the lower limit of multiplication for which TCPH analysis will work and identify potential improvements to experiment design by investigating the effects of neutron scatter on analysis results.

These contributions have the potential to be a useful tool in nuclear warhead verification. Classifying an object as multiplying or non-multiplying in the context of a fast neutron image provides necessary verification information without compromising sensitive source parameters.

1.3   Organization

This dissertation is organized as follows:

Chapter 2 (Background and Analysis Methods) describes the concepts and tools used in this research. It begins with a description of fission chain reactions possible in a multiplying assembly and how the gammas and neutrons released in such events are detected and identified in organic scintillators. These concepts lead to an explanation of time-correlated pulse-height (TCPH) analysis, the methodology by which assemblies may be classified as multiplying. The chapter concludes with an introduction to coded aperture imaging, a description of the Neutron Coded Aperture Imager (NCAI), and the method used to estimate source intensity in a fast neutron image. The NCAI is the system used to perform measurements analyzed in this work.

Chapter 3 (Experiment Analysis) describes a series of experiments performed at the Nevada Nuclear Security Site (NNSS), and the results of applying TCPH analysis to measurements conducted with the NCAI. The experiments involved both multiplying and non-multiplying sources, arranged separately and together in three separate scenes. The first scene, containing both sources together, demonstrates the ability to correctly classify sources as multiplying in a scene containing multiple sources. The second and third scenes, containing the individual sources separately, demonstrates

15

that the success of the method in the first scene was not due to the difference in relative source strengths.

Chapter 4 (Simulation Analysis) summarizes Monte Carlo simulations performed to predict the outcome of two series of experiments. The first series was performed to estimate the lower limit of multiplication for which the methodology successfully identified multiplying material; results are presented for solid and hollow spheres of weapons grade plutonium metal. The second series was performed to investigate of the effect of neutron scatter on TCPH analysis and identify potential improvements to experiment design. Results for this series are presented for increased neutron scatter within the detector field-of-view and for decreased neutron scatter outside the detector field-of-view.

Chapter 5 (Conclusions and Future Work) summarizes the results of and offers conclusions about this work, including the expected limits of applicability for the methodology. Finally, topics of future work are identified.

CHAPTER

2

BACKGROUND AND

ANALYSIS METHODS

The aim of this research is to differentiate between multiplying and non-multiplying sources in fast neutron images. The distinction is important because multiplying, or fissile, materials are capable of sustaining fission chain reactions [25] and are used as the fuel in nuclear explosives. This chapter provides an overview of the concepts necessary to achieve this goal by describing neutron-induced fission and fission chain reaction characteristics (where the gammas and neutrons of interest come from), neutral particle detection in organic scintillators (how the gammas and neutrons are detected), and particle type identification (how to tell the difference between the gammas and neutrons). The time-correlated pulse-height analysis technique, a method by which

fast neutrons from fission chain reactions are identified and multiplying materials are classified, is then described in detail. Finally, the chapter concludes with a description of coded aperture imaging, the neutron coded aperture imager, and the fast neutron image analysis techniques used in this research.

2.1 Fission Chain Reactions

A neutron-induced fission reaction involving parent nucleus X and daughter nuclei Y and Z can be represented by

$$_x^a X + _0^1 n \rightarrow _y^b Y + _z^c Z + \nu _0^1 n + G\gamma, \tag{2.1}$$
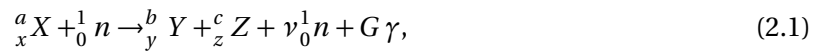
where $a + 1 = b + c + \nu$ and $x = y + z$ must hold true in order to conserve nucleons and protons respectively. There are over 3,300 known nuclides, but less than 60 will undergo thermal neutron[1]-induced fission. Nuclides with a thermal neutron-induced fission cross section are shown in Figure 2.1 [5]. Of these, only ^{235}U and ^{239}Pu are used as fuel in nuclear weapons.
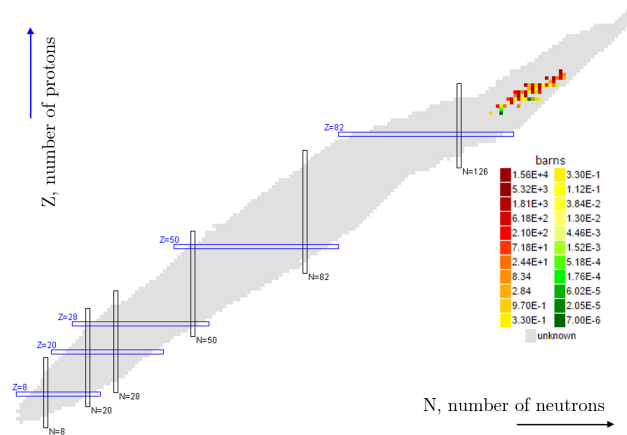
Figure 2.1 Chart of nuclides. The gray area represents nuclides that have no thermal neutron-induced fission cross section; those with the cross section are colored [5].

---

[1] A neutron with kinetic energy of 0.025 eV.

The values for b, c, and ν in Equation 2.1 are not uniquely determined because the masses b and c follow a bi-modal mass-yield distribution specific to the parent nuclide and incident neutron energy [22]. The mass-yield distributions for thermal neutron-induced fission for ^{235}U and ^{239}Pu are shown in Figure 2.2 [4].
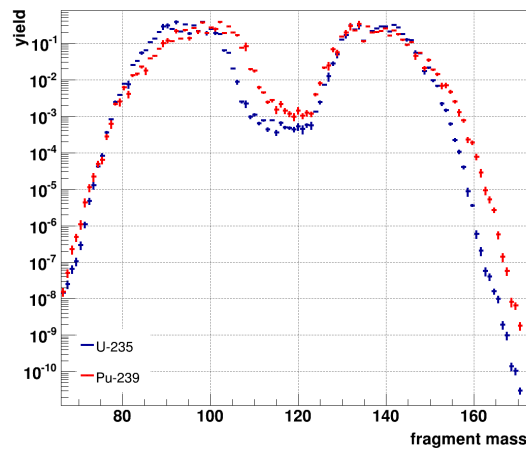
Figure 2.2 Mass-yield distributions. The mass-yield distributions for thermal neutron-induced fission are shown for (blue) ^{235}U and (red) ^{239}Pu.

The ν prompt neutrons are emitted within 0.1 femtoseconds of the fission [22]. The number ν of prompt neutrons emitted follows a Gaussian distribution with mean $\overline{\nu}$ and standard deviation $\sigma \approx 1.1$ for most fissile nuclides. The mean number of prompt neutrons emitted during fission $\overline{\nu}$ is a property of the fissioning nucleus, with typical values falling between two and three neutrons [48]. The prompt neutron energy distribution may be represented by either a Maxwell or Watt fission spectrum, depending on the parent nucleus and incident neutron energy, with a mean energy of about 2 MeV. The neutron spectra for thermal neutron-induced fission for ^{235}U and ^{239}Pu are shown in Figure 2.3.

19
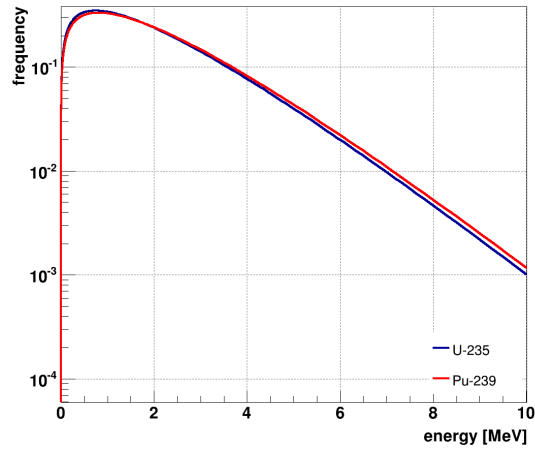
Figure 2.3 Fission neutron spectra. The neutron spectra for thermal neutron-induced fission are shown for (blue) ^{235}U and (red) ^{239}Pu.

The G prompt gammas are also emitted within 10 femtoseconds of the fission [22]. The number distribution of prompt gammas emitted G is not as well characterized as its neutron counterpart ν, but several simulation codes such as MCNPX, MCNP6, and Geant4 employ a negative binomial distribution with a mean $\overline{G}$ of about eight gammas per fission [52]. The prompt gamma fission energy distribution may be represented by a piecewise empirically fit function with a mean value of about 900 keV [41] [51] [52]. The empirically fit gamma spectrum for thermal neutron-induced fission of ^{235}U is shown in Figure 2.4; this is the spectrum sampled for spontaneous and induced fission in the MCNPX, MCNP6, and Geant4 simulation codes [52].

A fission chain reaction is comprised of multiple generations: a neutron born from a fission may induce another fission event in a subsequent generation. The multiplication factor for an infinite medium k_∞ is defined as the ratio of neutrons produced by fission in one generation to the number of neutrons produced by fission in the preceding generation. When taking into account source geometry and loss mechanisms such as absorption and leakage, this quantity becomes the effective multiplication factor k [7]. This quantity is a measure of the degree to which a source material

20
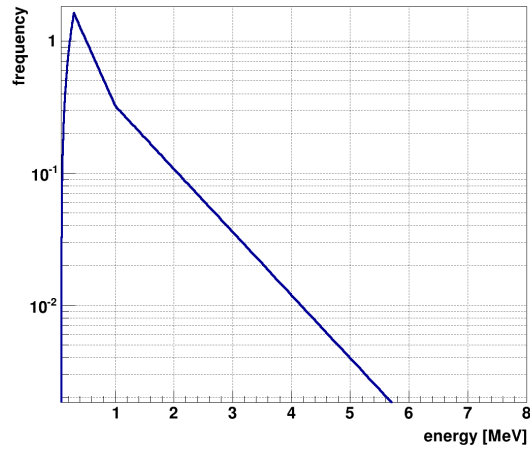
Figure 2.4 Fission gamma spectra. The gamma spectra for thermal neutron-induced fission is shown for ^{235}U.

arranged in a particular geometry will sustain a chain reaction. A subcritical assembly will have $k < 1$, indicating a chain reaction occurs but gradually dies away. In terms of the total number of neutrons produced by a chain reaction, the neutron multiplication M is

$$M = 1 + k + k^2 + k^3 + \cdots, \tag{2.2}$$

which is a geometric series that converges to

$$M = \frac{1}{1-k}, \quad k < 1. \tag{2.3}$$

Neutron multiplication is the expected number of neutrons produced in a subcritical assembly for each incident source neutron. As a non-fissile material cannot support fission chain reactions, $k = 0$ and therefore $M = 1$; this type of neutron source is non-multiplying. Conversely, fissile material is multiplying and will have $M > 1$.

The average prompt neutron lifetime ℓ for fissile material in metallic form, such as what would

21

be found in a nuclear explosive, is on the order of 10 nanoseconds [14]. This quantity is the time between a neutron's birth in a fission and its subsequent absorption. In a multiplying assembly, this absorption could result in another fission as part of a chain reaction; the time difference between fissions is the neutron generation time Λ. This quantity is the ratio of the prompt neutron lifetime to the multiplication factor, or

$$\Lambda = \ell/k. \tag{2.4}$$

The neutron generation time therefore is on the order of 10 to 100 nanoseconds for $k \in [0.1, 1.0]$. In terms of neutron multiplication, the neutron population in a subcritical assembly as a function of time $n(t)$ is

$$n(t) = n_0 \exp\left(\frac{k-1}{\ell} \cdot t\right) = n_0 \exp\left(\frac{-t}{M\ell}\right), \tag{2.5}$$

where n_0 is the neutron population at $t = 0$. It is apparent in Equation 2.5 that a higher multiplication leads to a more gradual reduction in the neutron population.

The detection of a correlated gamma-neutron pair from different generations of a fission chain reaction is the basis of time-correlated pulse-height analysis; this technique of identifying multiplying assemblies is discussed in detail in Section 2.4.

2.2 Organic Scintillators

Organic scintillators, which consist of aromatic hydrocarbons primarily in benzenoid rings, convert the kinetic energy of charged particles to visible light via energy transitions within the molecular electronic structure of the scintillating material [21]. Because gammas and neutrons are neutral particles, their detection requires an intermediate reaction that produces charged particles.

Compton scattering is the main mode of gamma interaction with atoms of low atomic number and therefore the mechanism by which incident gammas produce charged particles in an organic

22

scintillator. The recoil electrons emerging from Compton scatter have energy E_e determined by

$$E_e = \left[1 - \frac{1}{1 + (1 - \cos\theta)E_\gamma/m_e c^2} \right] \cdot E_\gamma, \tag{2.6}$$

where E_γ is the energy of the incident gamma, θ is the angle of the scattered gamma, and $m_e c^2$ is the electron rest mass energy. Maximum energy transfer from the incident gamma to the recoil electron occurs when $\theta = 180°$.

Elastic scattering by hydrogen nuclei is the main mode of neutron interaction in an organic scintillator. The recoil proton produced in a neutron elastic scatter has energy E_p determined by

$$E_p = \left[1 - \frac{(1 + \alpha) + (1 - \alpha)\mu}{2} \right] \cdot E_n, \quad \alpha = \left(\frac{A - 1}{A + 1} \right)^2. \tag{2.7}$$

E_n is the energy of the incident neutron, μ is the cosine of the scatter angle in the center-of-mass frame, and A is the mass number of the recoiling nucleus. Elastic neutron scatter is isotropic in the center of mass frame; i.e., the probability distribution $p(\mu)d\mu$ is uniformly distributed on the interval $[-1, 1]$. An incident neutron can impart all its energy to a hydrogen nucleus (a proton, $A = 1$) when scattering 180°; on average, it imparts half its energy.

The recoiling charged particle (electron or proton) then deposits energy in the detector medium by exciting molecular electronic states as illustrated in Figure 2.5. Energy is absorbed by a molecule in the ground state, placing the molecule in a singlet state with net electric spin $s = 0$. It may de-excite to one of the vibrational states of the ground state by emitting a photon (prompt fluorescence), or undergo inter-system crossing to a triplet state with net electric spin $s = 1$. Prompt fluorescence occurs on a time scale on the order of nanoseconds. From the triplet state, the molecule could gain energy such that it reoccupies a singlet state and then de-excites (delayed fluorescence). Delayed fluorescence occurs on a time scale on the order of hundreds of nanoseconds [21].

Recoil electron energy is converted to light in a linear relationship. However, the conversion of

المنارة للاستشارات

www.manaraa.com
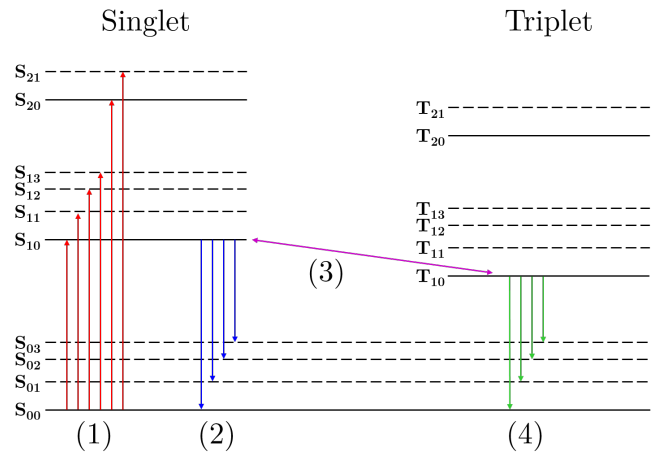
Figure 2.5 Example scintillator molecule electronic structure. The solid black lines represent electronic energy levels and the dashed horizontal black lines represent vibrational sub-levels, with S and T indicating singlet and triplet states, respectively. The red arrows (1) represent absorption, the blue arrows (2) represent fluorescence, the purple arrow (3) represents inter-system crossing, and the green arrows (4) represent phosphorescence. Adopted from Knoll [21].

recoil proton energy is nonlinear due to quenching processes, e.g., molecular damage and triplet annihilation, because these do not produce light. The light yield differences are compared on an absolute basis by expressing the recoil proton light output in MeV electron equivalent (MeVee), or the light output produced by a 1MeV electron [21]. The light output conversion for recoil protons used in this work is described in Section 2.7.

The light produced in these interactions is then converted into an electrical signal by a photodetector, e.g., a photomultiplier tube (PMT). The PMT anode pulse can then be analyzed to identify the particle type (gamma or neutron) of the incident radiation. This classification is done on a per pulse basis and is discussed in the next section.

24

2.3 Particle Type Identification

The relative amount of delayed light produced differs for incident gammas and neutrons; virtually all light from electron excitation comes from prompt fluorescence. The number of molecules excited to the longer-lived triplet states is proportional to the energy loss per unit distance traveled (dE/dx) of the exciting particle [21]. Because the recoil protons produced by neutron elastic scatter have higher dE/dx, light produced by incident neutrons will have a larger component from delayed fluorescence relative to light produced by incident gammas; this difference is shown in Figure 2.6(a).

<div align="center">(a)   (b)</div>
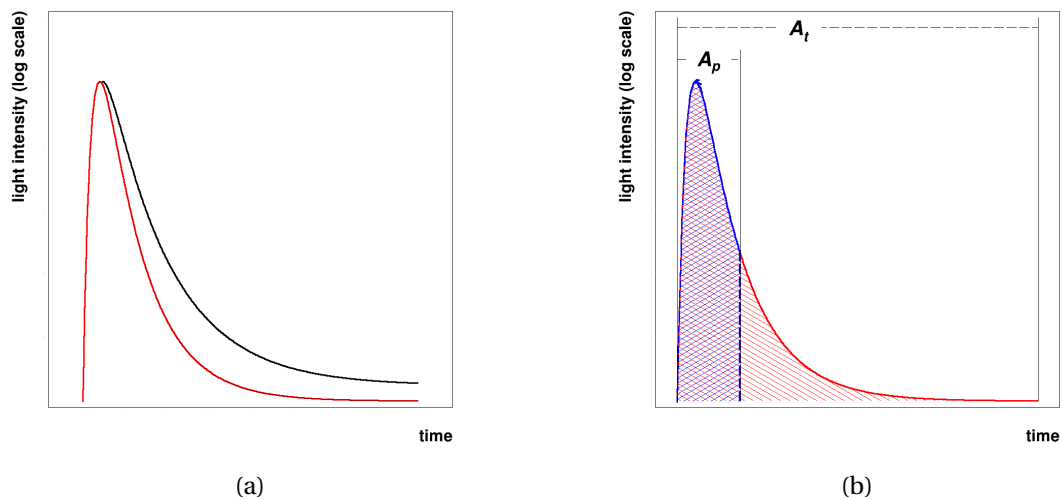
Figure 2.6 Idealized pulse shape behavior and analysis. (a) Idealized pulse behavior in an organic scintillator for a (red) gamma-induced event and the (black) relatively larger component from delayed fluorescence from a neutron-induced event. (b) Example charge integration intervals used in particle identification with (red) total area and (blue) prompt area.

The charge integration technique of particle type identification makes use of this difference in pulse shape for different species of incident radiation. A pulse shape discrimination (PSD) parameter can be calculated from the ratio of the prompt to total pulse areas; these areas for an example pulse

are illustrated in Figure 2.6(b). Neutrons will have a lower PSD parameter due to the larger slow

component relative to a gamma pulse with the same total area. An example PSD parameter vs. pulse

height histogram from a measurement of weapons grade plutonium performed with an EJ-299

plastic scintillator is shown in Figure 2.7(a).

<div align="center">(a)   (b)</div>
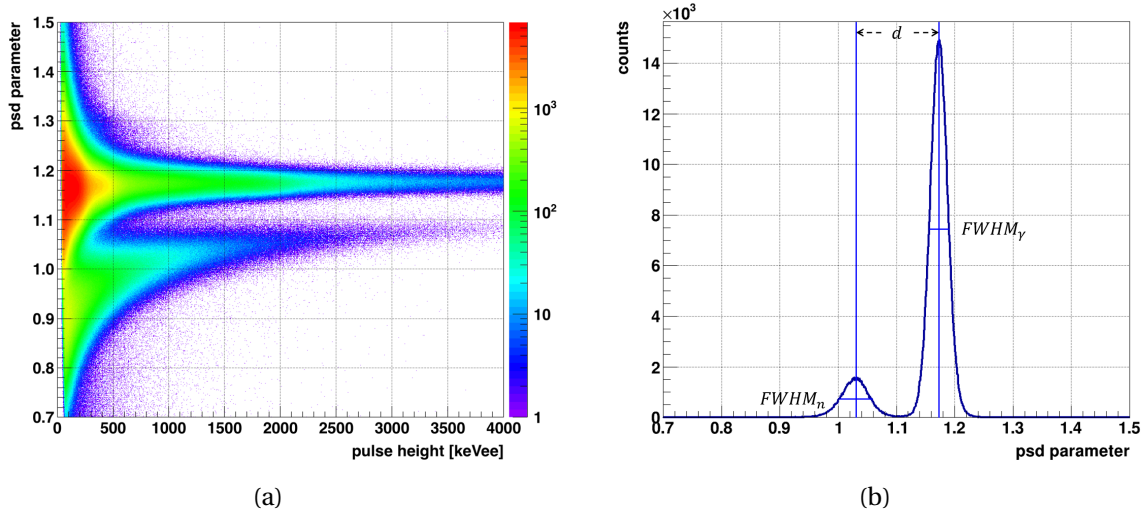
Figure 2.7 Particle type identification and PSD figure of merit. (a) An example PSD parameter vs. pulse height histogram from a measurement performed with an EJ-299 plastic scintillator shows separation between gammas (top band) and neutrons (bottom band). This separation is due to the pulse shape differences and PSD parameter calculation illustrated in Figure 2.15. (b) The PSD parameter distributions for pulse height 1000 to 1500 keVee illustrates the parameters used in calculating a PSD figure-of-merit.

The end time for the prompt area integration is typically optimized for a specific scintillator and

PMT combination to produce the greatest PSD parameter separation for neutrons and gammas of

equal total area. This optimization uses a figure of merit FOM defined as

$$FOM = \frac{d}{FWHM_n + FWHM_\gamma},$$ (2.8)

where d is the separation between the PSD distribution means and $FWHM$ is the full width at

half maximum of the distributions for neutrons (n) and gammas (γ). A horizontal projection of Figure 2.7(a) for pulse height 1000 to 1500 keVee is shown in Figure 2.7(b) to illustrate the quantities used in calculating a PSD figure-of-merit.

2.4 Time-Correlated Pulse-Height Analysis

Time-correlated pulse-height (TCPH) analysis is a technique used to assess source multiplication by examining the relationship between neutron pulse height and kinetic energy estimated from time-of-flight [31].

This technique requires the detection of a correlated gamma-neutron pair. In the discussion that follows, detected gamma-neutron pairs are assumed to be correlated; the consequences of relaxing this assumption are described in the next section. For a correlated gamma-neutron pair, both particles either emerge from (a) the same fission, or (b) different generations of the same fission chain reaction. Figure 2.8 depicts the basic experiment setup used to conduct TCPH analysis. The setup consists of a fissioning source placed a distance d away from two organic scintillator detectors capable of particle type identification.
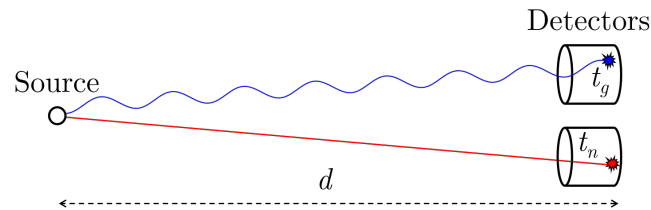
Figure 2.8 Basic TCPH experiment setup. A correlated (blue) gamma and (red) neutron are detected in sequence at times t_g and t_n, respectively.

The apparent neutron time-of-flight Δt is estimated by using the gamma detected immediately prior to the neutron to estimate the time of the fission event. The time of the fission event t_f occurs

27

at the absolute time of the gamma detection event t_g, minus the time it took for the gamma to travel from the source to the detector, or

$$t_f = t_g - \frac{d}{c}, \tag{2.9}$$

where c is the speed of light. The apparent neutron time-of-flight is then the absolute time of the neutron detection event t_n, minus the time of the fission event, or

$$\Delta t = t_n - t_f = t_n - \left(t_g - \frac{d}{c} \right). \tag{2.10}$$

The apparent neutron kinetic energy E_n, based on equation 2.10, is therefore

$$E_n = \frac{1}{2} m_n \left(\frac{d}{\Delta t} \right)^2, \tag{2.11}$$

where m_n is the mass of the neutron.

The apparent neutron kinetic energy E_n estimated in Equation 2.11 is an upper bound on energy deposition ΔE in the scintillator, as discussed in Section 2.2. The light output due to the recoil proton is

$$L(\Delta E) = 0.75\Delta E - 3.2[1 - \exp(-0.22\Delta E)], \tag{2.12}$$

where L is the light output in electron-equivalent units, ΔE is the energy deposited by the neutron via a neutron-proton collision, and the coefficients are detector-specific, experimentally determined constants for EJ-299 organic scintillators [24]. The light output calibration curve used in this work is shown in Figure 2.9(a).

A plot of light output (pulse height) vs. apparent time-of-flight, illustrated in Figure 2.9(b), provides a means to detect fission chain reaction neutrons, and therefore identify a multiplying assembly. The red line is where the light output L is equal to the light output corresponding to full deposition of the apparent neutron kinetic energy $L(\Delta E = E_n)$ for a single fission event. For a

28
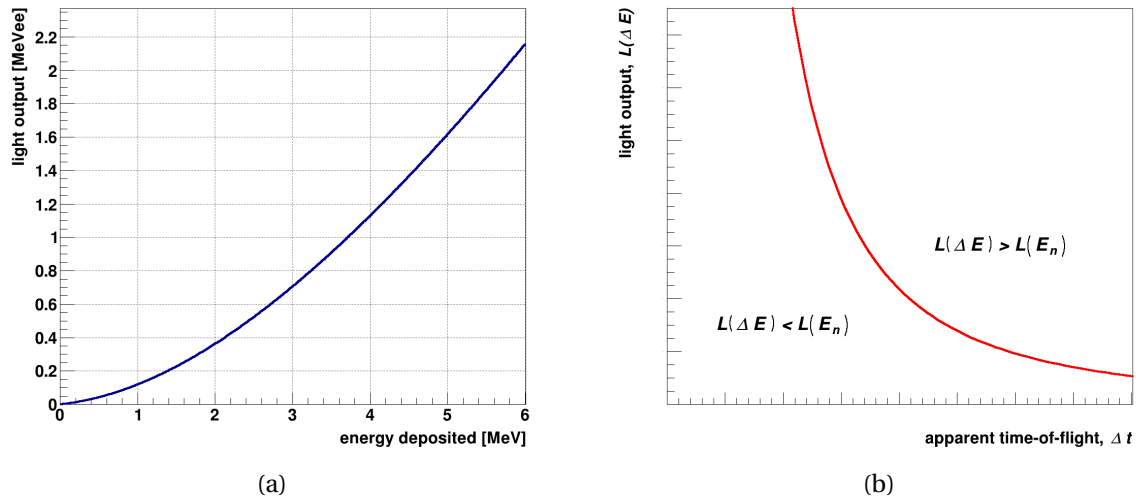
Figure 2.9 Light output calibration curve and TCPH histogram. (a) The conversion of neutron energy deposition to light output was conducted using Equation 2.12 with calibration constants for EJ-299 organic scintillators [24]. (b) The light output is used in a TCPH histogram to detect fission chain reaction neutrons. The red line is where the pulse height L is equal to the light output corresponding to full energy deposition of the apparent neutron kinetic energy $L(\Delta E = E_n)$.

correlated gamma-neutron pair, the two possible detection scenarios are depicted in an idealized geometry in Figure 2.10.

The first case, shown in Figure 2.10(a), shows the detection of a gamma-neutron pair from a single fission. In this scenario, the observed pulse height L must be less than or equal to the light output corresponding to the apparent neutron kinetic energy $L(E_n)$; i.e., the energy deposited in the detector cannot exceed the apparent kinetic energy. Thus, single fission events depicted in this scenario will appear in Figure 2.9(b) only on or below the red line.

However, in a multiplying medium, it is also possible to have the second case shown in Figure 2.10(b). This scenario shows the detection of a gamma born in a fission event and the subsequent detection of a correlated neutron from a later generation of a fission chain reaction. In this case, the neutron can have a larger apparent time-of-flight than can be accounted for in the light output; i.e., its measured pulse height will be larger than possible if it were emitted simultaneously with the

29
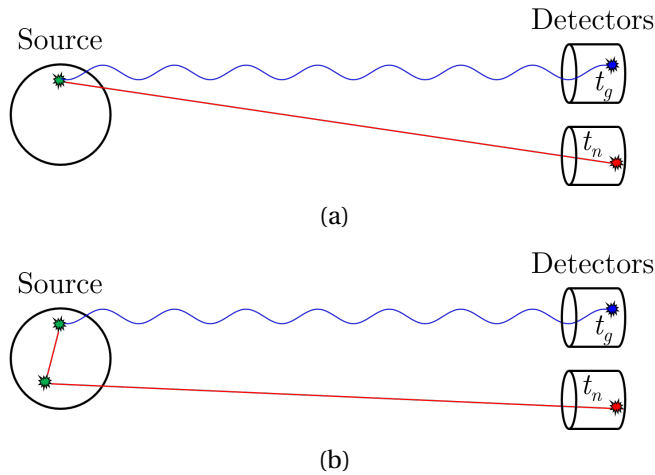
Figure 2.10 Idealized TCPH detection scenarios are shown for a correlated gamma-neutron pair from (a) a single fission and (b) different generations of a fission chain reaction.

gamma in a single fission. Because this relationship is only possible for a correlated gamma-neutron pair from different generations in a fission chain reaction, events appearing above the red line in Figure 2.9(b) are evidence of a fission chain reaction.

The red line in Figure 2.9(b) is therefore a discrimination line that effectively divides a pulse height vs. apparent time-of-flight histogram into two regions: events on or below the line are both single fission and fission chain reaction neutrons, while events above the line are only fission chain reaction neutrons.

2.5   Complicating Factors in TCPH Analysis

The description of the TCPH analysis methodology assumed the detection of a fission-correlated gamma-neutron pair in an idealized experiment setup. In practice, these are not the only event pairs detected [34], and experiments are seldom conducted under ideal conditions. This section discusses the implications of relaxing these assumptions using Figure 2.11 to illustrate various effects.
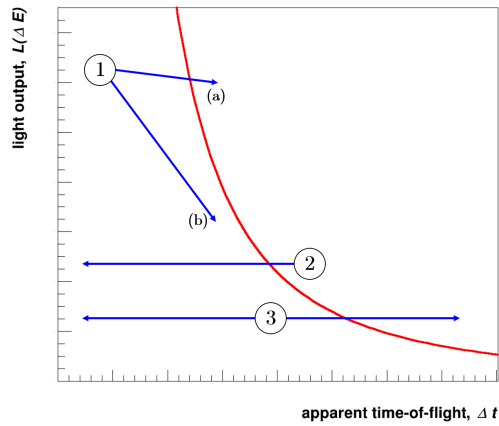
Figure 2.11 Complicating factors in TCPH analysis. Path (1) shows the effects of neutron scatter with (a) heavy nuclei and (b) light nuclei. Path (2) shows the effect of inelastic scatter near the detector. Path (3) indicates that accidental coincidences appear in the histogram on both sides of the discrimination line.

2.5.1   Path 1: Neutron Scatter

A neutron that scatters before reaching the detector will arrive later than it would otherwise, leading to a longer apparent time-of-flight estimate; this is shown in path 1 in Figure 2.11. The increase in apparent time-of-flight is dependent on the neutron kinetic energy and its trajectory from the source to the detector. The decrease in light output is dependent on the mass of the scattering nucleus, as described by Equation 2.7.

Path 1(a) illustrates a slight decrease in light output, which is most likely if the scatters occur with heavy nuclei. In these scatters, very little energy is lost; e.g., a neutron loses on average only 1% of its energy per scatter with a lead nucleus. The scenario represented by path 1(a) introduces the possibility that the neutron appears to the right of the TCPH discrimination line when it should not; i.e., a correlated gamma-neutron pair from a single fission event could appear as a fission chain reaction event. The impact of such misclassification is investigated in Chapter 4.

Alternatively, path 1(b) illustrates a large decrease in light output, which is most likely if the scatters occur with light nuclei. In these scatters, the neutron can lose a great deal of energy; e.g., a

31

neutron loses on average 50% of its energy per scatter with a hydrogen nucleus (a proton). The scenario represented by path 1(b) does not impact the results of TCPH analysis because the correlated gamma-neutron pair still appears as a single fission event.

2.5.2   Path 2: Inelastic Scatter

A neutron that experiences an inelastic scatter near the detector could produce a gamma whose detection is used to estimate the neutron time-of-flight. The effect of this scenario would be to make the neutron appear to arrive earlier than it would otherwise, moving the event left on the pulse height vs. time-of-flight histogram. This scenario is illustrated by path 2 in Figure 2.11 and is discussed further in Chapter 4. Inelastic scatter near the detector does not impact the results of TCPH analysis.

2.5.3   Path 3: Accidental Coincidences

Gamma-neutron pairs in which the two particles are uncorrelated arise when the detected gamma is born in a fission event in a different chain, as a result of nuclear decay, or as a result of a neutron capture event. These gamma-neutron pairs are accidental coincidences and are shown in path 3 in Figure 2.11. In these cases, the gamma and neutron are independent and these are Poisson random events [21].

Accidental coincidences are not necessarily problematic because it possible to estimate the accidental coincidence rate by examining data collected at long (e.g., microsecond scale) time-of-flight where real coincidences are essentially impossible. The estimated mean accidental coincidence rate can be subtracted from the TCPH histogram in a manner analogous to background subtraction in gamma spectroscopy. This process is described in Chapter 3.

2.6   Coded Aperture Imaging

A camera with a single small pinhole is capable of producing a high resolution image with a low signal-to-noise ratio. A larger pinhole would increase the signal-to-noise ratio, but only at the expense of spatial resolution. Coded aperture imaging is a method that can produce images with both high resolution and signal-to-noise ratio. These benefits are realized by using a mask consisting of many pinholes in an aperture pattern, effectively creating an encoded picture of many overlapping low intensity, high resolution images that must be subsequently decoded [3, 10]. This process is illustrated in Figure 2.12 [10].
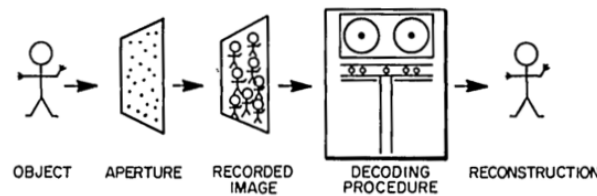
Figure 2.12 Coded aperture imaging process. Source radiation is spatially modulated by the aperture pattern in a mask to form an encoded image. The recorded image can then be decoded to form a reconstructed object image. The illustration is from [10].

The decoding process is represented mathematically through a series of correlation operations. For Equation 2.13 and Equation 2.14, spatial coordinates are represented by (k, l) in the imaging plane and (i, j) in the aperture and object planes. In the discrete case, the encoded picture $P(k, l)$ is formed by the correlation of an object $O(i, j)$ and the aperture pattern $A(i, j)$, plus some noise $N(k, l)$, or

$$P(k, l) = \sum_i \sum_j O(i, j) A(i + k, j + l) + N(k, l). \tag{2.13}$$

The noise term includes any signal not modulated by the aperture pattern of the mask. In the encoding process, $A(i, j)$ is a binary array that represents the opacity of the mask (+1 for open

33

elements and 0 for closed elements), while $P(k, l)$ is the measured image intensity. The correlation operation is used again in order to create a reconstructed object image $\hat{O}(i, j)$, except this time with a decoding array $G(i, j)$, or

$$\hat{O}(i, j) = \sum_k \sum_l P(k, l)G(k + i, l + j). \tag{2.14}$$

In the decoding process, $G(i, j)$ is the complement of $A(i, j)$; i.e., each open element is +1 and each closed element is −1, with the central element being set to +1 [11]. By defining $G(i, j)$ this way, its correlation with $A(i, j)$ approximates a delta function. Imperfections in decoding may be attributed to imperfect alignment of the mask projection onto the detector pixels, i.e., the mask pattern does not line up with the detector segmentation. The correlation of 19 element aperture pattern with its decoding array is shown in Figure 2.13 as an example.
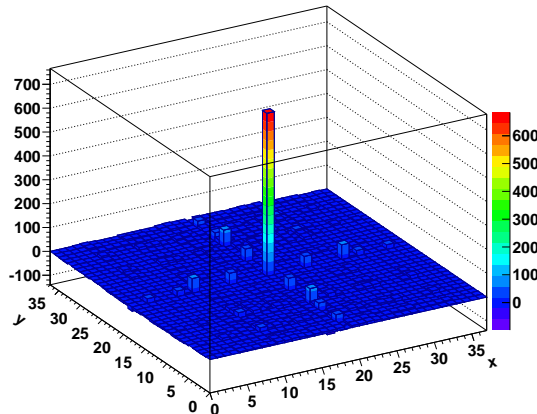
Figure 2.13 Correlation of an aperture pattern with its decoding array. The correlation of a 19 element aperture pattern with its decoding array is shown.

The process described above is a general description of coded aperture imaging. Fast neutron coded aperture imaging employs the same method, but requires suitable mask and detector choices.

34

The mask must be constructed with a material capable of modulating fast neutrons; a polyethylene mask serves this purpose by down-scattering fast neutrons to energies below the detection threshold. The detectors that record the encoded image must be capable of detecting fast neutrons, and they must be constructed or arranged in such a way as to identify position of interaction in the imaging plane. Organic scintillators with particle type identification capabilities, as discussed in Section 2.2 and Section 2.3, are the best choice for fast-neutron coded aperture imaging.

2.7   Neutron Coded Aperture Imager

The neutron coded aperture imager (NCAI), shown in Figure 2.14, was designed and built in a joint project between Oak Ridge and Sandia National Laboratories. It employs a polyethylene mask that modulates fast neutrons and uses plastic scintillators capable of identifying the position of interaction in the imaging plane and particle type.

The mask, shown on the left side of Figure 2.14(a), is a rank 19 anti-symmetric modified uniformly redundant array (MURA) [19]. The mask is constructed of two 2.54 cm thick layers of high-density polyethylene stacked with a 1.5 cm thick layer of borated polyethylene closest to the detector array. Incident neutrons are modulated by downscattering to energies below the detection threshold. Rotating the mask 90° interchanges the open and closed portions; i.e., the mask rotated by 90° is its own anti-mask. This arrangement is beneficial because background sources not in the NCAI field of view are eliminated by taking the difference between mask and anti-mask measurements. The relative positions of the mask and detector assembly may be adjusted to adjust the object plane field-of-view [17].

The detector array is shown on the right side of Figure 2.14(a). It is composed of a 4×4 array of block detectors, one of which is shown in Figure 2.14(b). The active volume of each detector is a $10.8 \times 10.8 \times 5 \, cm^3$ block of EJ-299-34 plastic scintillator, optically subdivided by specular reflector film into a 10×10 pixel array. The scintillator is coupled through an acrylic light guide to four

35
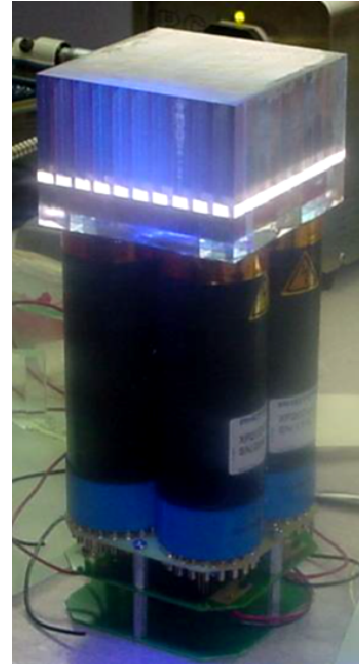
(a)   (b)

Figure 2.14 The neutron coded aperture imager (NCAI). (a) The detector assembly is shown in the back-ground encased in black and the rotating mask is shown in the foreground. (b) One block detector consists of an EJ-299-34 optically segmented plastic scintillator block atop an acrylic light guide coupled to four PMTs.

photomultiplier tubes (PMTs). The pixel of interaction inside the block detector is determined using Anger logic, whereby the (k, l) position is interpolated from the relative responses of the four PMTs. The 4×4 array of block detectors therefore contains 40×40 pixels covering an approximately $45 \times 45 \, \text{cm}^2$ area. Each aperture on the mask is resolved by four detector pixels; the encoded picture image is double-sampled.

Particle type identification is accomplished by analyzing a histogram of PSD parameter vs. pulse height, with the PSD parameter calculated as the ratio of prompt to total light collected. An example histogram showing each particle type band is shown in Figure 2.15, which also shows the associated mean and standard deviation as a function of light output. The gamma and neutron PSD parameter distributions for narrow intervals of energy deposition are fit with two Gaussian distributions to

36

estimate the mean and standard deviation for each particle type band [38]. Every point in the histogram can therefore be expressed in terms of number of standard deviations away from each particle type mean, allowing the user to set tolerances for particle type identification based on the energy-dependent width of that particle's PSD parameter distribution.
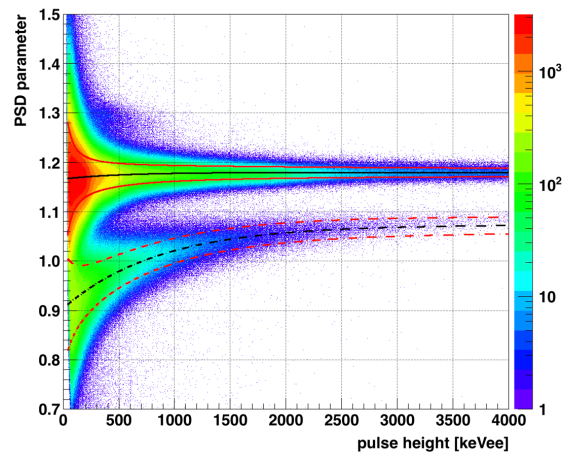
Figure 2.15 Particle identification with the NCAI. The black lines indicate the mean values of the (solid) gamma and (dashed) neutron PSD parameter distributions. The red lines indicate the (solid) gamma and (dashed) neutron 1σ locations.

The NCAI records the charge collected by the photomultiplier tubes (which is directly proportional to light output), pixel number, and absolute time of interaction. Additionally, the PSD parameter and particle type identification parameters are calculated and recorded. This information is stored in ROOT n-tuples for offline analysis [37]. The NCAI ROOT structure is shown in Figure 2.16.

37
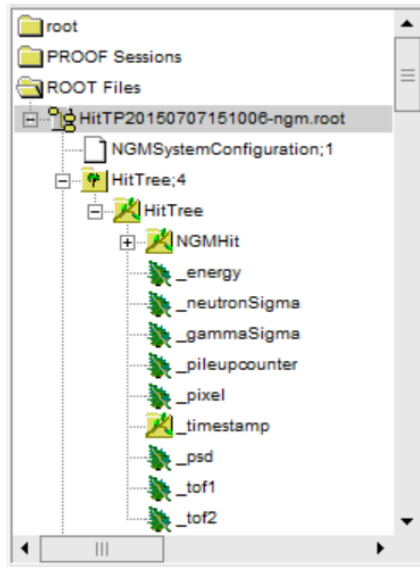
Figure 2.16 NCAI ROOT structure. The NCAI stores the charge collected (_energy), pixel number (_pixel), time of interaction (_timestamp), PSD parameter (_psd), and particle identification parameters (_neutronSigma and _gammaSigma) in ROOT n-tuples.

2.8   Estimating Source Intensity and Uncertainty in an Image

A region of interest (ROI) may be defined in a reconstructed image as an area containing a source. The source intensity is estimated by summing the counts of each pixel in the ROI. In the case of an ROI in a double-sampled reconstructed image, this sum is divided by four so that the counts along a basis vector are correct. The example fast neutron image shown in Figure 2.17 illustrates estimating the counts attributed to a source in an ROI. The image shown is reconstructed from a measurement of a ^{252}Cf point source.
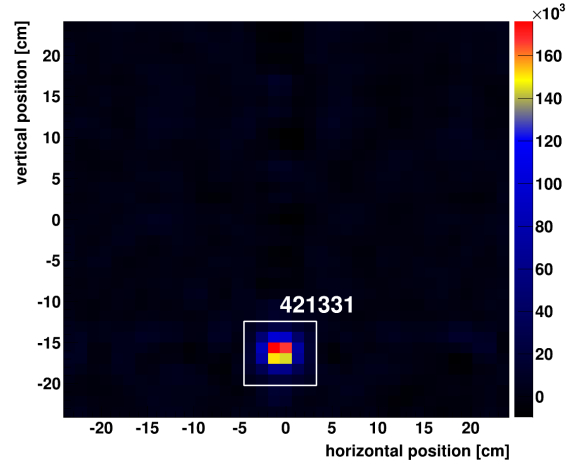
Figure 2.17 Estimating counts in a region of interest. The source intensity was estimated by summing the counts in each image pixel and dividing by four.

The following discussion of estimating the uncertainty in an ROI sum was originally presented by Fleenor [11]. The variance of a single reconstructed object image pixel $\sigma^2_{\hat{O}(i,j)}$ is determined by linear propagation of uncertainty:

$$\sigma^2_{\hat{O}(i,j)} = \sum_k \sum_l \left(\frac{\partial \hat{O}(i,j)}{\partial P(k,l)} \right)^2 \sigma^2_{P(k,l)}. \tag{2.15}$$

Each encoded picture pixel $P(k,l)$ is assumed to be independent and is Poisson distributed. Examination of Equation 2.14 shows the partial derivative term is the decoding array, which, since it is squared, evaluates to unity for all values of (k,l). Additionally, since each $P(k,l)$ is assumed to be Poisson distributed, $\sigma^2_{P(k,l)} = P(k,l)$; therefore the variance of a single object image pixel is equal to the total number of counts in the detector.

The reconstructed object image pixels, however, are not independent. Therefore, when estimating source strength in an ROI by summing multiple object image pixels, the covariance between these pixels must be taken into account. For two pixels $\hat{O}(i,j)$ and $\hat{O}(u,v)$, the variance of the sum

39

$\sigma^2_{\hat{O}(i,j)+\hat{O}(u,v)}$ is given by

$$\sigma^2_{\hat{O}(i,j)+\hat{O}(u,v)} = \sigma^2_{\hat{O}(i,j)} + \sigma^2_{\hat{O}(u,v)} + 2\sigma^2_{\hat{O}(i,j)\hat{O}(u,v)}. \tag{2.16}$$

The covariance term is dependent on mask rank, whether or not mask and anti-mask data are used in reconstructing the object image, and whether or not the encoded picture is double-sampled. In the case of the NCAI, the normalized covariance is 0.5 for pixels that share an edge and 0.25 for pixels that share a corner[2] [11]. The total variance for an ROI is therefore determined by accounting for the variance of each pixel, as well as its covariance with each of its nearest neighbors.

Figure 2.18(a) shows the contribution of each pixel in the ROI to the estimated variance of the ROI sum, normalized to the variance of a single pixel. Figure 2.18 illustrates the estimate of the uncertainty in the ROI when including the covariance term; not accounting for the covariance among pixels in the ROI results in an uncertainty of 1548 counts.

The next chapter demonstrates the application of TCPH analysis to selectively reconstruct fast neutron coded aperture images using fission chain reaction neutrons.

---

[2]These coefficients have been normalized to the variance of a single pixel and are for reconstructing an object image using mask and anti-mask data sets.
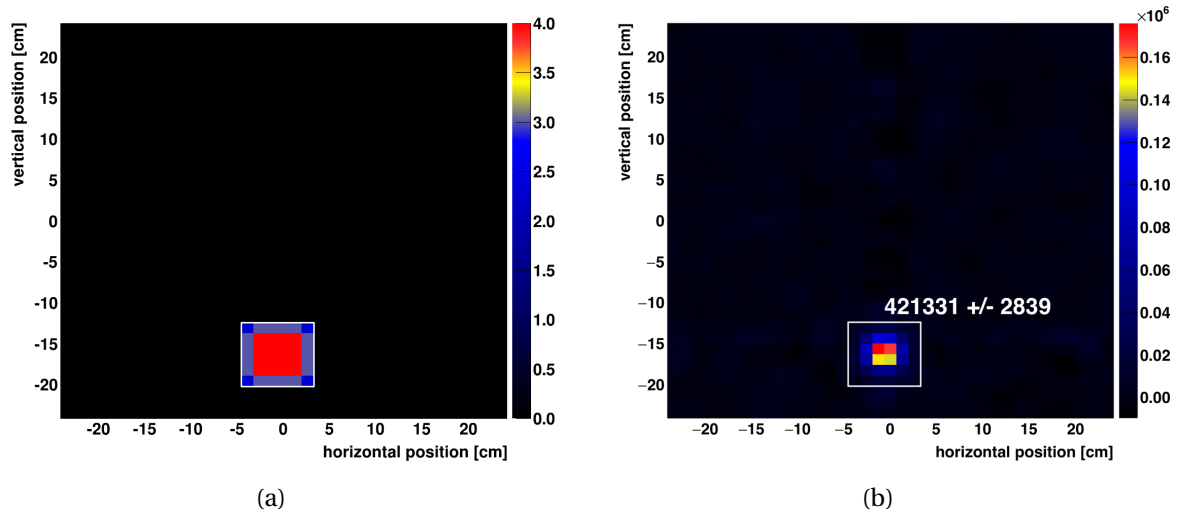
Figure 2.18 Estimating uncertainty in a region of interest. (a) The contribution of each pixel to the variance, normalized to the variance of a single pixel, is shown. (b) The uncertainty shown was estimated by applying Equation 2.16 to each pair of adjacent pixels in the ROI.

41

CHAPTER

3

EXPERIMENT ANALYSIS

North Carolina State University and Oak Ridge National Laboratory conducted experiments with special nuclear material (SNM) in the Device Assembly Facility (DAF) at the Nevada National Security Site (NNSS) in summer 2015 [30]. These experiments used multiplying and non-multiplying sources together and separately to acquire fast neutron images using the neutron coded aperture imager (NCAI). Sandia National Laboratories conducted an additional experiment involving a non-multiplying source using the NCAI at Sandia in January 2016 [2].

3.1 Experiment Design

The multiplying source used in this series of experiments was the BeRP[1] ball, which is a 7.5 cm diameter sphere of 4.5 kg α-phase plutonium metal encased in a 0.3 mm thick stainless steel shell. The BeRP ball is 94% ^{239}Pu and 6% ^{240}Pu. It has a multiplication of about 4.5 and emits approximately 8.8×10^5 neutrons per second[2] [29, 34]. The BeRP ball was measured in a bare configuration; i.e., without any shielding or moderating materials surrounding the source. A picture and schematic of the BeRP ball is shown in Figure 3.1.
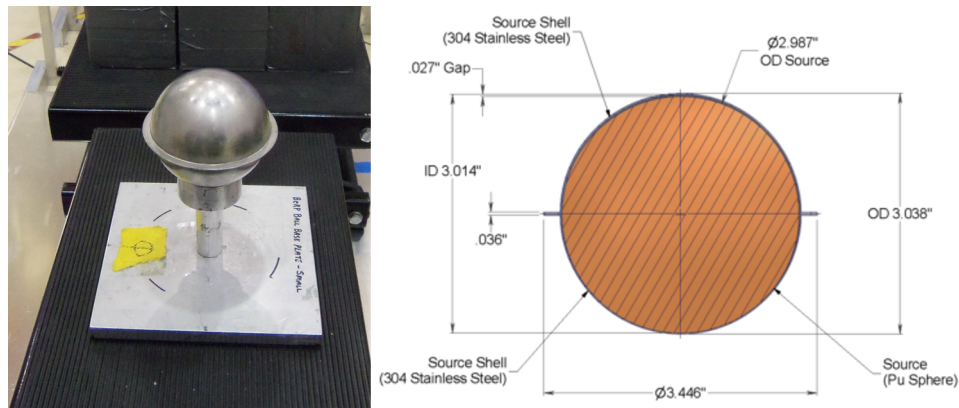
Figure 3.1 BeRP ball. The BeRP ball was placed on an aluminum stand during measurements, as shown in the picture on the left. The schematic is from [29].

A 76 μCi ^{252}Cf point source was used as the non-multiplying spontaneous fission source in the DAF experiments. At the time of the experiment (July 6, 2015), this source emitted 3.3×10^5 neutrons per second. A 23 μCi ^{252}Cf point source was used in the Sandia experiment conducted in January 2016.

---

[1]BeRP stands for Beryllium-Reflected Plutonium. One of the first experiments conducted with the BeRP ball was the evaluation of the reactivity worth of beryllium reflectors [29].

[2]This rate is the neutron leakage rate, or the neutron production rate times the neutron leakage probability for the assembly.

These sources were measured together and separately in three scenes. In each scene, the object plane was 70.5 cm from the center of the NCAI aperture, which was 61 cm from the rear of the detector volume (image plane). A sketch of this geometry is shown in Figure 3.2. The three measured scenes were:

- Scene 1 contained both the BeRP ball and the ^{252}Cf source.

- Scene 2 contained only the ^{252}Cf source.

- Scene 3 contained only the BeRP ball.
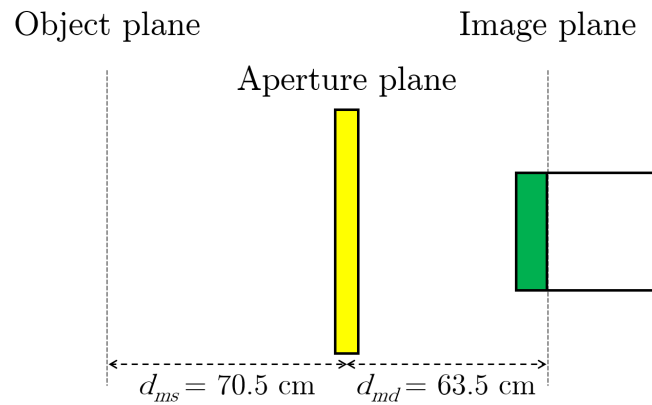
Figure 3.2 Experiment geometry. The source placement established the object plane (left), and the NCAI placement established the the aperture plane (yellow, middle) and the scintillator detector volume (green, right) locations. This sketch is not to scale.

Scenes 1 and 3 were measured at the DAF and each measurement lasted one hour. Scene 2 was measured at Sandia with a measurement time of 196 minutes, i.e., about three times longer. The longer measurement time was chosen so the image contained the same number of counts from the ^{252}Cf as the DAF measurement.

44

3.2   Analysis Procedure

This section uses the scene 1 measurement data as the illustrative example to describe the analysis procedure. Scenes 2 and 3 were analyzed in the same way.

3.2.1   Particle Identification

Gammas were defined as having a PSD parameter p within two standard deviations σ_γ of the gamma PSD parameter mean $\overline{p}_\gamma$. This condition is described by

$$\left| \frac{p - \overline{p}_\gamma}{\sigma_\gamma} \right| \leq 2. \tag{3.1}$$

Similarly, neutrons were defined as having a PSD parameter within two standard deviations σ_n of the neutron PSD parameter mean $\overline{p}_n$ and more than five standard deviations σ_γ from the gamma PSD parameter mean $\overline{p}_\gamma$. This is described by

$$\left| \frac{p - \overline{p}_n}{\sigma_n} \right| \leq 2 \quad \text{and} \quad \frac{p - \overline{p}_\gamma}{\sigma_\gamma} \leq -5. \tag{3.2}$$

Additionally, a low-energy threshold of 125 keVee was applied for both particle types. The threshold eliminates the area of the PSD parameter distributions with the most overlap, sets the neutron energy that the mask modulates, and ensures a common threshold for all detector pixels. This light output corresponds to a neutron energy of about 1 MeV. PSD parameter vs. pulse height histograms before and after the application of these conditions is shown in Figure 3.3.

3.2.2   Reconstructing a Fission Chain Reaction Neutron Image

A two-dimensional histogram of counts in each pixel forms the encoded picture $P(k, l)$ used in Equation 2.13 and Equation 2.14. A neutron image is created by analyzing each recorded event

45
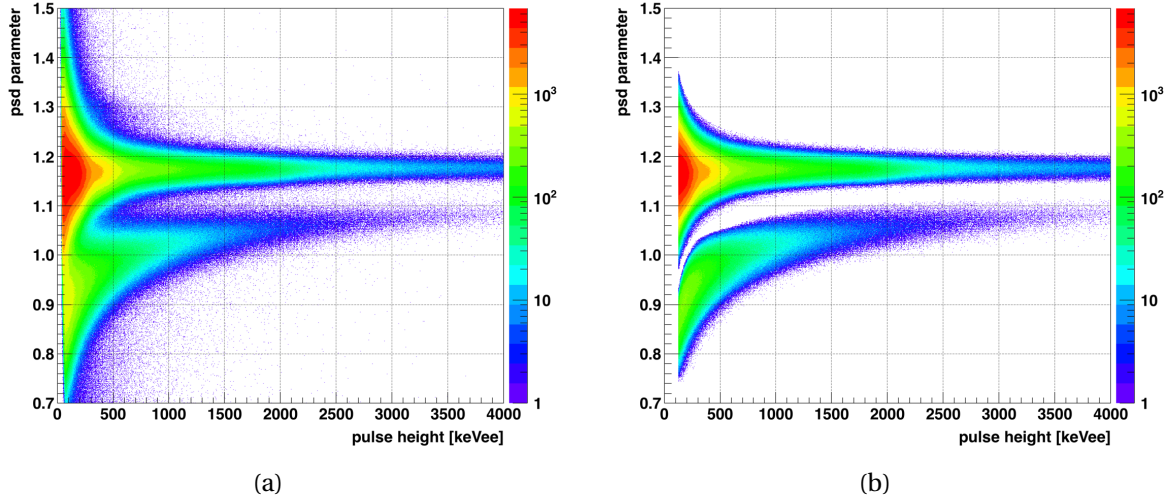
Figure 3.3 Particle type identification. PSD vs. pulse height histograms (a) before and (b) after the application of particle type identification conditions. Events in the top band are gammas and the bottom band are neutrons.

and accumulating $P(k, l)$ using only events that meet the neutron identification criteria; this reconstruction is referred to as the original image. To create an image of neutrons born in fission chain reactions, $P(k, l)$ is accumulated using only events that meet the TCPH analysis criteria. This "TCPH filter" accepts neutrons that deposit more energy than predicted by their apparent time-of-flight and rejects all others. The standard neutron imaging and TCPH filter methodologies are illustrated in Figure 3.4 and the filter is described in the remainder of this section.

The apparent time-of-flight Δt for each neutron is estimated using the preceding gamma to estimate the time of fission as described in Equation 2.10. In order to construct a TCPH filter, the observed apparent time-of-flight is shifted by subtracting the expected time-of-flight based on the neutron energy deposited in the scintillator; for positive values, the resulting quantity can be described as the excess time-of-flight relative to a single fission event. The excess time-of-flight Δt_{ex} was determined by

$$\Delta t_{ex} = \Delta t - \sqrt{\frac{m_n d^2}{2\Delta E}}, \tag{3.3}$$

46
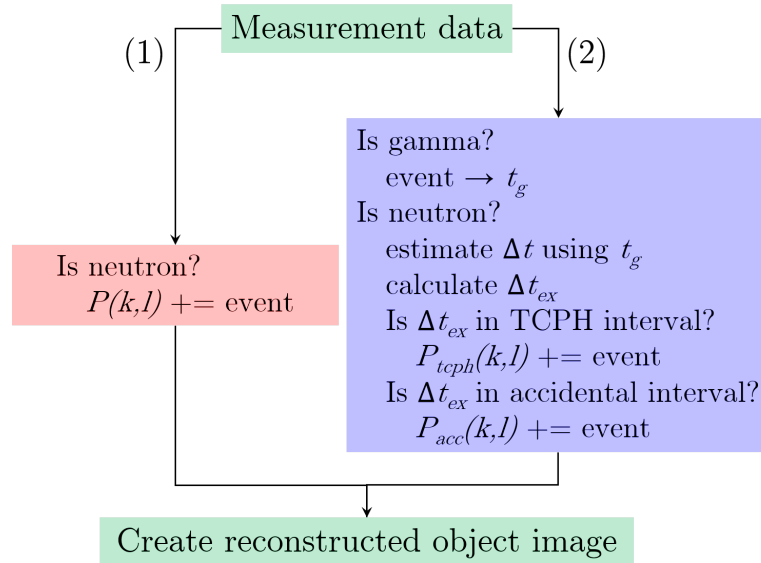
Figure 3.4 Standard neutron imaging and TCPH filtering methodology. The standard neutron imaging loop is shown in path 1 (left), while the TCPH filtering loop is shown in path 2 (right). Both loops examine each event in the measurement data to form the encoded image histogram $P(k,l)$. The time Δt_{ex} shown in path 2 is the excess time-of-flight relative to a single fission event.

where m_n is the neutron mass, the distance d is distance from the center of the source to the rear of the imaging plane[3], and ΔE is the neutron energy deposited in the scintillator. The effect of this shift is that the energy dependence of the discrimination line illustrated in Figure 3.5(a) is removed, and it becomes a vertical line centered at $\Delta t_{ex} = 0$. The lower time boundary of the TCPH filter is therefore $\Delta t_{ex} = 0$ and events to the left of this line are discarded. The resulting histogram of pulse height vs. excess time-of-flight is shown in Figure 3.5(b).

An upper time boundary of the TCPH filter is needed to prevent the reconstructed image from being dominated by accidental coincidence events. This upper boundary is determined by examining a vertical projection of the excess time-of-flight TCPH histogram. Vertical projections of Figure 3.5(b) are shown in Figure 3.6. In these histograms, the accidental interval is defined to

---

[3]The distance from the source to the corner of the imaging plane is used because it is the longest possible flight path. This distance yields the smallest estimate of Δt_{ex} such that classification of fission chain reaction neutrons is conservative.
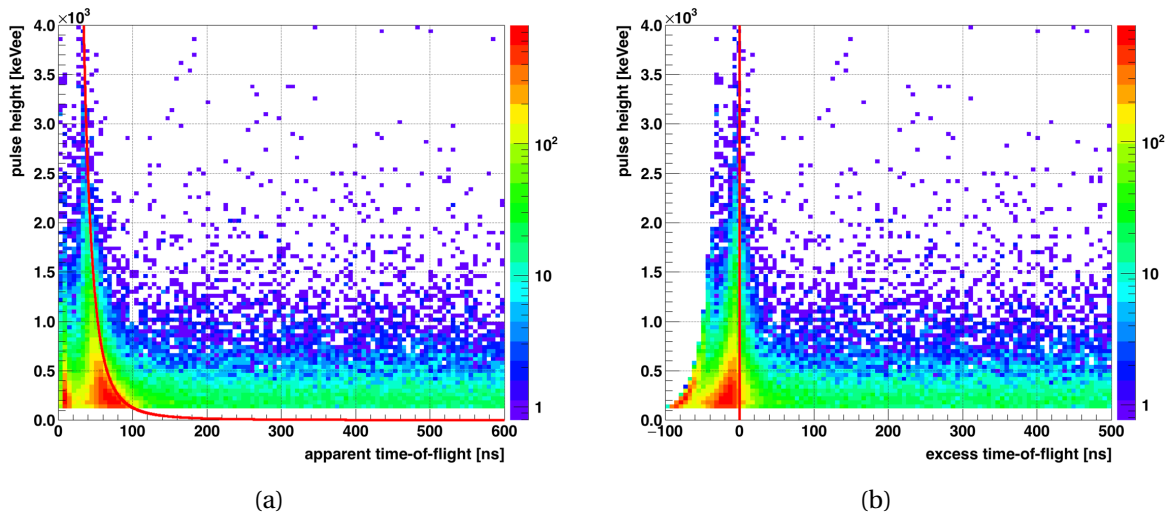
Figure 3.5 Time-of-flight histograms. (a) The original apparent time-of-flight histogram and the (b) shifted excess time-of-flight histogram are shown. The red line indicates the TCPH discrimination line in each.

be $\Delta t_{ex} = (10 \text{ to } 100)\mu s$, and Figure 3.6(a) shows an exponential fit over this region in green. The inter-arrival time in this interval is a Poisson process as discussed in Section 2.5.3, and therefore exponentially distributed. The red lines in Figure 3.6 are a back projection of this fit, representing the accidental coincidence contribution to the histograms for smaller values of excess time-of-flight.

The counts above the red line in Figure 3.6(b) are attributed to fission chain reactions, and the line is the expected accidental rate. The upper time boundary of the TCPH filter was selected to maintain a high fission chain-to-accidental ratio FAR, determined by

$$FAR = \frac{\sum\limits_{t=0}^{t'} N(t) - \int\limits_{0}^{t'} f(t)\,dt}{\int\limits_{0}^{t'} f(t)\,dt}, \tag{3.4}$$

where $N(t)$ is the observed counts at excess time-of-flight t and $f(t)$ is the functional form of the accidental coincidence fit[4]. The fission chain-to-accidental ratio was evaluated for t' starting at the

---

[4]The functional form is $f(t) = \exp(a + b \cdot t)$. The coefficients a and b are the fit parameters.
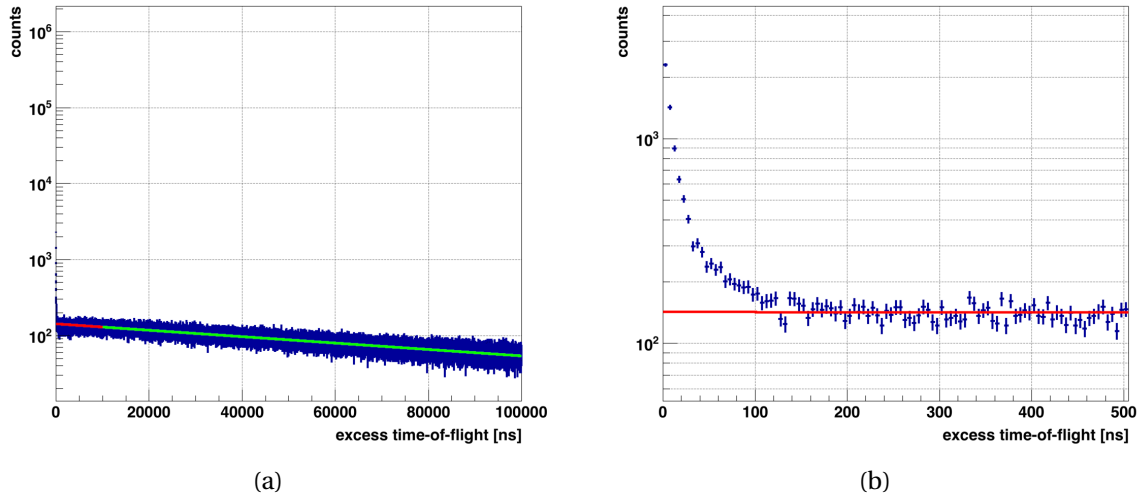
Figure 3.6 Time interval analysis histograms. These histograms are vertical projections of Figure 3.5(b), showing (a) wide and (b) narrow excess time intervals. The green line in (a) is a fit over a region consisting of accidental coincidence events and the red line in both subfigures is a back projection of the fit.

first positive histogram bin center and was incremented by the histogram bin width. The excess time-of-flight corresponding to a FAR of 2.5 was found to produce satisfactory results for all three experiment scenes examined when used as the upper time boundary of the TCPH filter. Plots of the FAR analysis and the results of applying the TCPH filter to Figure 3.5(b) are shown in Figure 3.7.

3.2.3 Accidental Coincidence Subtraction

The events depicted in the Figure 3.7(b) histogram form the TCPH-filtered encoded picture $P_{tcph}(k, l)$, which is then used to reconstruct an image containing fission chain reaction neutrons; however, the resulting image also contains accidental coincidence events. Those events are eliminated by forming an encoded picture $P_{acc}(k, l)$ using events in the accidental region ($\Delta t_{ex} = (10 \text{ to } 100)\mu$s), reconstructing an accidentals image, and subtracting a scaled version from the TCPH-filtered image. The scaling factor x used for the accidentals image is the ratio of the areas under the accidental fit

49
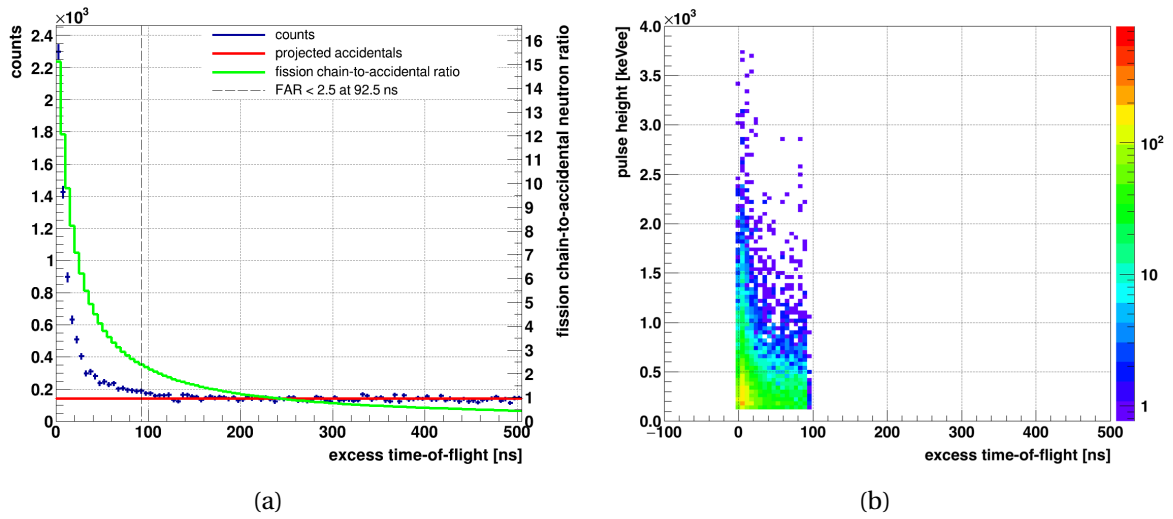
Figure 3.7 TCPH filter upper time boundary and filter application. The (a) FAR analysis shows the ratio falls below 2.5 at 92.5 ns and (b) shows the results of the applying the TCPH filter to the excess time-of-flight histogram.

in each region, or

$$x = \frac{\int_{0}^{t_{FAR}} f(t)\,dt}{\int_{10\,\mu\text{s}}^{100\,\mu\text{s}} f(t)\,dt}, \tag{3.5}$$

where t_{FAR} is the upper time boundary from the FAR analysis and $f(t)$ is the functional form of the accidental fit. This progression of images is shown in Figure 3.8.

3.2.4   Identifying a Multiplying Assembly

The original image containing all neutron events is analyzed to determine regions of interest (ROI) containing fast neutron sources. These same ROIs are examined in the final image reconstructed using only fission chain reaction neutrons. An estimate of source intensity and its uncertainty in the final image is made using the techniques discussed in Section 2.8; the statistical significance of the source in each ROI is determined by the ratio of the counts N in the ROI to its uncertainty

50
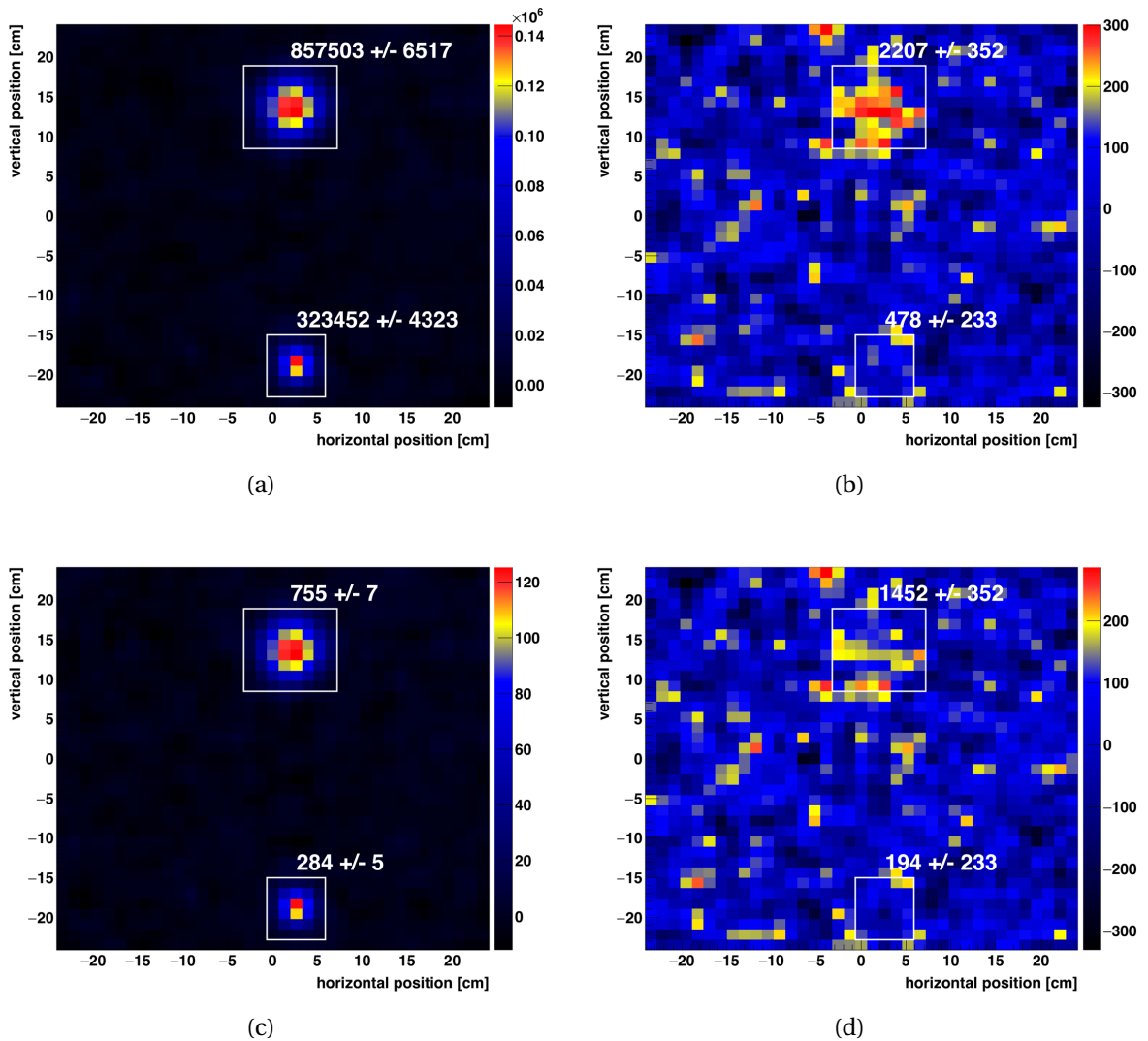
Figure 3.8 Images used in applying the TCPH filter. The (a) original image is analyzed to determine regions of interest containing sources. The TCPH filter is applied to the measurement data, forming the (b) TCPH-filtered image. A (c) scaled image using events from the accidental region is then subtracted from (b) to form the (d) final image consisting of only fission chain reaction neutrons. The numbers above each region of interest are the estimated counts within the region and associated uncertainty.

σ. This work classifies the sources identified in the original image as multiplying if the statistical significance of the source in the final image is greater than one.

51

3.3 Scene 1: BeRP Ball and ^{252}Cf Source

In this scene, the BeRP ball was placed on a short pedestal resting on top of a lab jack stand and the ^{252}Cf source was placed on the base of the lab jack stand. The vertical distance between the two sources was 30 cm. A picture of this source placement is shown in Figure 3.9.
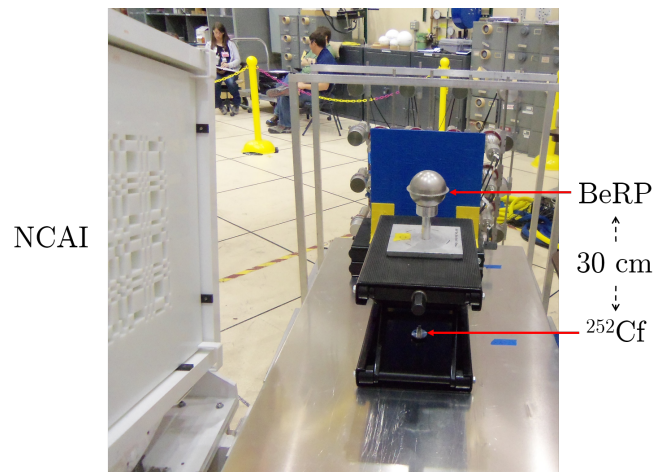
Figure 3.9 Scene 1 source placement. The BeRP ball was arranged 30 cm above the ^{252}Cf source. A portion of the NCAI aperture is visible on the left.

The fast neutron image reconstructed from all detection events for this scene is shown in Figure 3.10(a). It is evident in this image that there are two neutron sources present, the top source being more spatially distributed and approximately 2.7 times more intense than the bottom source; however, this image by itself does not indicate if either source is a multiplying assembly. Figure 3.10(b) is the fast neutron image reconstructed from only fission chain reaction neutrons for this scene. It is apparent that there is a fission chain reaction neutron source in the top portion of the image, but there are no indications that the second neutron source is present. It is possible to conclude that two neutron sources are present, and that only the top one is a multiplying assembly, when both images are viewed together and the same regions of interest are used.

Figure 3.10 Scene 1 results. The fast neutron images reconstructed from (a) all detection events and (b) only fission chain-reaction neutron events indicate there are two neutron sources present, but only the top source is a multiplying assembly.

3.4 Scene 2: ^{252}Cf Source Only

The multiplying source was approximately 2.7 times more intense than the non-multiplying source in scene 1. To demonstrate the removal of the ^{252}Cf source in the final image shown in Figure 3.10(b) was not a consequence of the difference in source intensities in scene 1, a ^{252}Cf source was measured separately. In this scene, the ^{252}Cf source was placed approximately 15 cm below the detector's central axis. The images reconstructed from all events and fission chain reaction events are shown in Figure 3.11; the image pair shows there is a neutron source present, but it is a non-multiplying assembly.

53
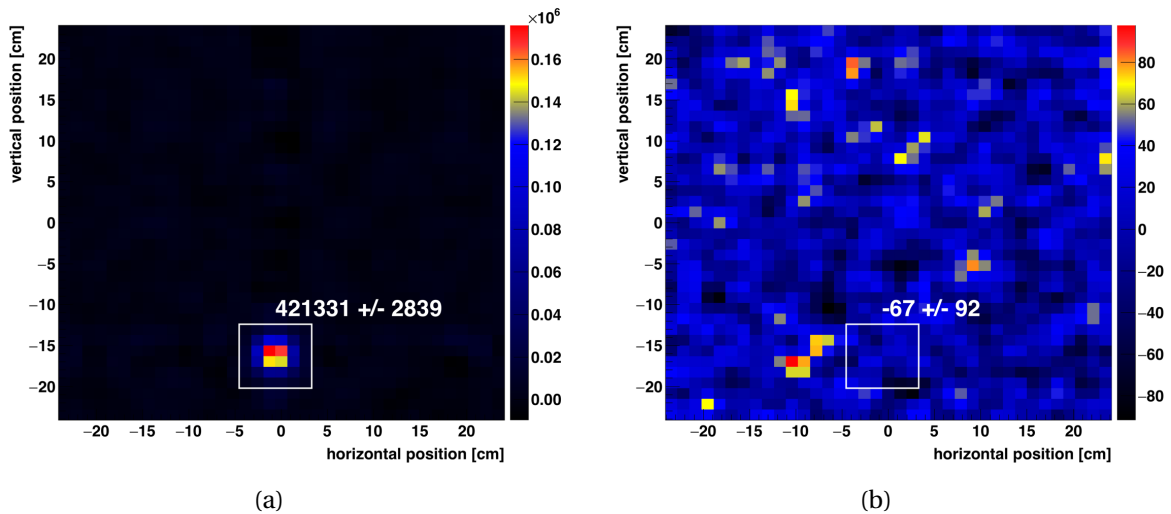
Figure 3.11 Scene 2 results. The fast neutron images reconstructed from (a) all detection events and (b) only fission chain-reaction neutron events indicate there is one neutron source present, but it is a non-multiplying assembly.

3.5 Scene 3: BeRP Ball Only

To demonstrate the TCPH filter does not remove a multiplying source when measured alone, the BeRP ball was measured separately. In this scene, the BeRP ball was placed on top of a short pedestal resting on an aluminum table. This placement, shown in Figure 3.12, was approximately 10 cm below the detector's central axis with a horizontal offset of about 12 cm. The images reconstructed from all events and fission chain reaction events are shown in Figure 3.13; the image pair shows there is a neutron source present and it is a multiplying assembly.

54

Figure 3.12 Scene 3 source placement. The BeRP ball was placed on a small pedestal resting on an aluminum table. The NCAI aperture is visible on the left.
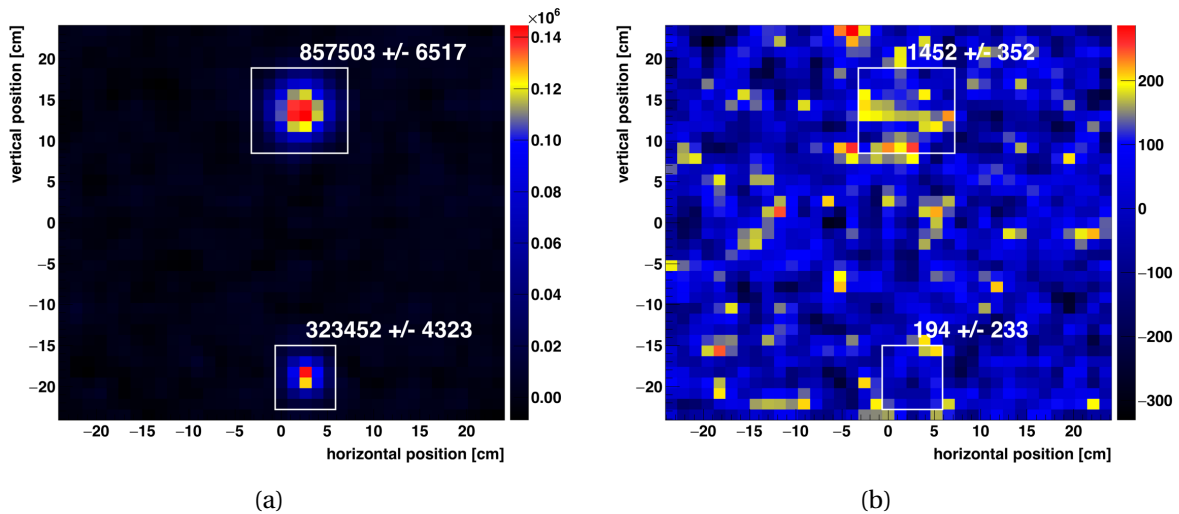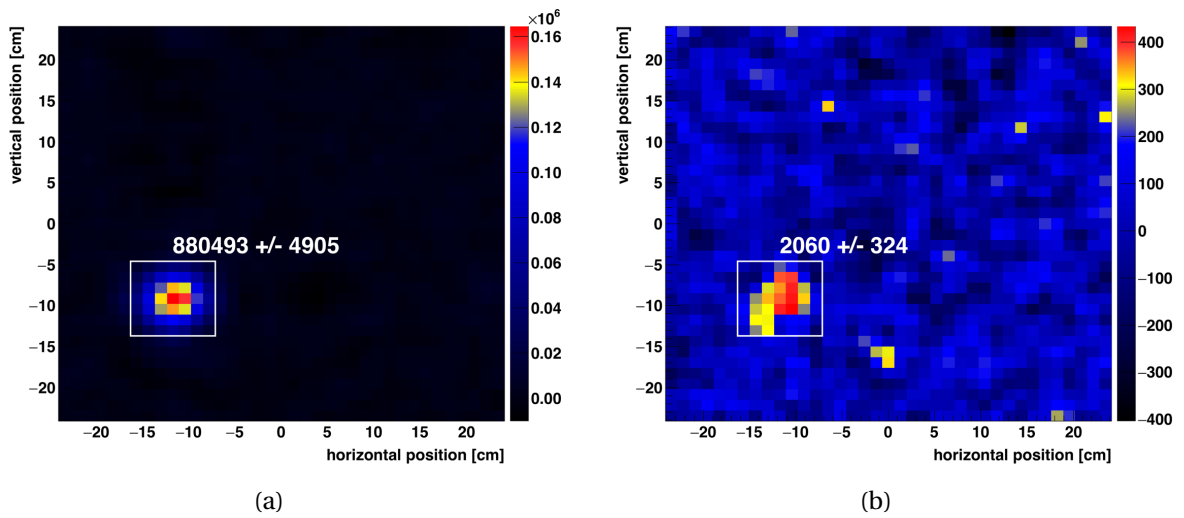

Figure 3.13 Scene 3 results. The fast neutron images reconstructed from (a) all detection events and (b) only fission chain-reaction neutron events indicate there is one neutron source present and it is a multiplying assembly.

3.6   Experiment Summary

Multiplying and non-multiplying sources were measured using the NCAI at the NNSS and Sandia National Laboratories. The sources were configured into three arrangements: the BeRP ball and ^{252}Cf source together (scene 1), the ^{252}Cf source alone (scene 2), and the BeRP ball alone (scene 3). For each measurement, a TCPH filter was applied and accidental coincidences were subtracted to create a fast neutron image containing fission chain reaction neutrons. The resulting image was analyzed in conjunction with the image formed using all neutron events to determine which, if any, of the sources were multiplying assemblies.

The analysis of the three scenes demonstrate it is possible to distinguish between multiplying and non-multiplying assemblies when the sources are imaged together or separately due to the dynamics of fission chain reactions. The differences in the excess time histograms for the ^{252}Cf source and BeRP ball are illustrated in Figure 3.14, where the increase in events to the right of the discrimination line for the BeRP ball may be attributed to the presence of fission chain reaction neutrons. A summary of the results for the three scenes is presented in Table 3.1.

Table 3.1 Summary of experiment results. The 'All events' and 'Fission chain reaction events' columns represent the estimated counts in the source regions of interest before and after applying TCPH analysis, respectively. The last column indicates the statistical significance of the source ROI in the final image formed using fission chain reaction neutrons.

Scene	Source	All Events	Fission Chain Reaction Events	N/σ
1	BeRP	$857,503 \pm 6,517$	$1,452 \pm 352$	4.1
	^{252}Cf	$323,452 \pm 4,323$	194 ± 233	0.8
2	^{252}Cf	$421,331 \pm 2,839$	-67 ± 92	-0.7
3	BeRP	$880,493 \pm 4,905$	$2,060 \pm 324$	6.4
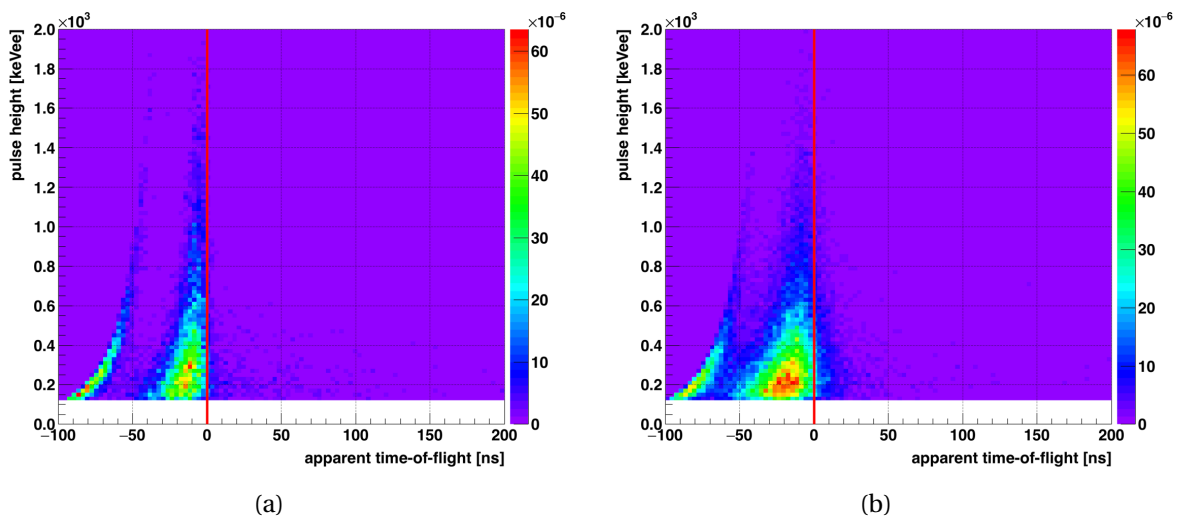
Figure 3.14 Scene 2 and scene 3 excess time histograms. The (a) scene 2 and (b) scene 3 excess time histograms, after subtracting accidentals and normalizing to total neutron counts in the detector, are shown.

57

CHAPTER

4

SIMULATION ANALYSIS

Three sets of Monte Carlo simulations were performed to investigate the limits of TCPH analysis and the effect of neutron scatter. The first set of simulations benchmarked the model against the scene 2 and scene 3 DAF measurements. Scene 2 contained only a ^{252}Cf source, while scene 3 contained only the BeRP ball.

The second set of simulations used weapons grade plutonium (WGPu) metal sources with the same composition and density as the BeRP ball. The simulations were performed to identify the lower limit of source multiplication for which TCPH analysis is successful; i.e., the minimum neutron multiplication a source must have to be preserved in a fission chain reaction neutron image. These simulations modeled both solid and hollow spherical WGPu assemblies.

The third set of simulations was performed to investigate the effect of neutron scatter in two

extreme scenarios. The first scenario involved a ^{252}Cf source in a highly scattering environment to determine if an increase in scattered neutrons could lead to misclassifying that source as multiplying. The second scenario involved the BeRP ball in a minimally scattering environment in an attempt to increase the contrast[1] of the chain reaction neutron image.

The simulations were conducted using MCNPX-PoliMi, an extension to the standard MCNPX Monte Carlo radiation transport code. MCNPX-PoliMi was designed to simulate fission correlation measurements [41] [39]. It samples neutron and gamma multiplicity and energy distributions during fission events and simultaneously produces multiple particles for single or chain reaction fissions. The simultaneous production of particles accounts for their correlation in time. The incident particle type, time, position, and energy deposited are recorded for each interaction in a set of user-specified cells.

4.1 Simulation Design

An MCNPX-PoliMi model[2] of the NCAI was used as the basis for simulation. A three-dimensional rendering of the model is shown in Figure 4.1. The model was adjusted to match the geometry of the DAF experiments shown in Figure 3.2. Gamma and neutron interactions in the 16 cells representing the active volume of the 4×4 array of EJ-299 plastic scintillator block detectors were recorded in the MCNPX-PoliMi collision log. Simulating a measurement involved seven steps:

1. Source creation and simulation.

2. Light output conversion and Gaussian smearing.

3. Conversion to absolute time and source combination.

4. Conversion of interaction position to pixel.

---

[1]Contrast in this context is the ratio of ROI counts to uncertainty, or the statistical significance at which a source appears in an image.

[2]The model was provided by Sandia National Laboratories.

5. Correction for detector dead time.

6. Particle identification.

7. Estimation of apparent time-of-flight and excess time.

Steps 1 and 6 are described in this section, while step 7 was performed as described in Section 3.2. Steps 2 through 5 are described in the appendix.
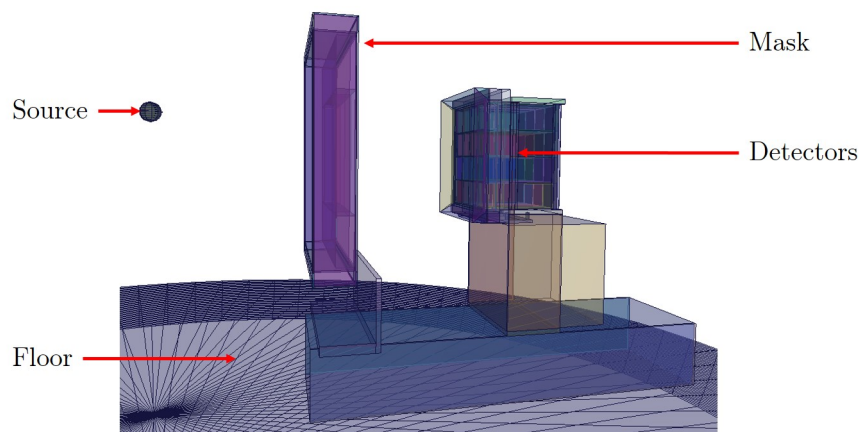
Figure 4.1 NCAI MCNPX-PoliMi model. The BeRP ball is shown on the left with the mask in the center and detector assembly on the right.

4.1.1 Source Creation and Simulation

The ideal simulated fissioning source would accurately model the prompt neutrons produced through fissions and delayed neutrons from fission products. It would also model the gammas from fissions, fission products, and α and β^- decay. MCNPX-PoliMi is capable of simulating ^{252}Cf and ^{240}Pu spontaneous fission sources; each history begins by sampling the neutron and gamma multiplicity and energy distributions specific to the radionuclide and emitting the particles simultaneously. Induced fissions produce neutrons and gammas in the same manner, and they are correlated to

60

the spontaneous fission event that started the chain reaction. These events determine the true coincidence rate in the simulation.

Delayed neutrons and gammas were not incorporated into the model. These particles are emitted at time scales characteristic of the half lives of their precursors. Precursor half lives are on the order of hundreds of milliseconds to tens of seconds, and so delayed particles would appear as accidental coincidences. Because delayed particle yields are a fraction of a percent of prompt yields, their exclusion will not impact the model [44].

The gamma emission rate due to α and β^- decay (subsequently referred to as "decay gammas"), however, is significant and has a noticeable effect on the accidental coincidence rate in the simulation. The importance of including the decay gammas in simulations of the BeRP ball is shown in the apparent time-of-flight histograms in Figure 4.2. In these histograms, the real coincidence rates under 200 ns are similar, but the accidentals are underestimated by an order of magnitude when the decay gammas are not included in the simulation. Because accidentals are subtracted when forming the image of chain reaction neutrons, underestimating the accidentals would lead to an overestimation of true coincidences and an underestimation of the uncertainty.

To account for decay gammas, the Bateman decay equations were solved to estimate the source composition at the time of the experiment [50]. The BeRP ball was manufactured by Los Alamos National Laboratory in 1980. It's americium and plutonium isotopic content, determined by analytical chemistry and mass spectrometry measurements at the time of its manufacture, is shown in Table 4.1 [29]. This composition was used as the initial condition for the Bateman decay equations to create a decay gamma spectrum for the BeRP ball on the date of the DAF experiments. The resulting decay gamma spectrum, which was generated from the plutonium composition and included the decay daughters, was then used as a MCNPX-PoliMi source term. This decay gamma source term contained 53 separate gamma energy distributions and was sampled according to their activity. Each model source therefore involved two separate simulations: one simulation replicating spontaneous fission (and any subsequent induced fission) and a second simulation replicating decay gammas.

61
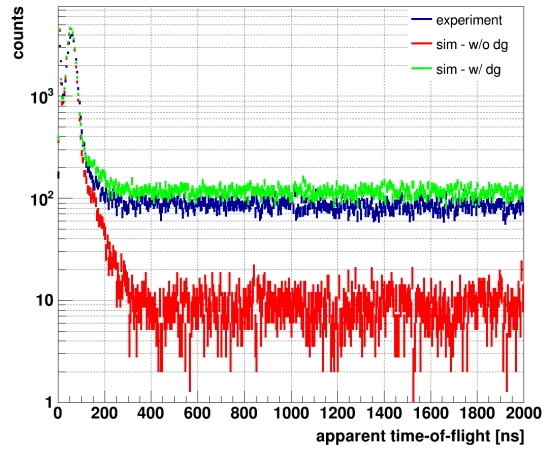
Figure 4.2 Decay gamma effect. The apparent time-of-flight histograms for the bare BeRP ball (blue) experiment, (red) simulation without decay gammas, and (green) simulation with decay gammas show the underestimation of the accidental rate when the decay gammas are not included.

Table 4.1 BeRP composition in 1980. This composition was used as the initial condition for the Bateman decay equations to determine the isotopic composition and decay gamma spectrum of the BeRP ball at the time of the DAF measurements.

Isotope	Mass Fraction [%]
^{238}Pu	0.020
^{239}Pu	93.74
^{240}Pu	5.95
^{241}Pu	0.269
^{252}Pu	0.028
^{241}Am	557 ppm

62

4.1.2 Particle Identification

MCNPX-PoliMi records the incident particle type for every interaction in user-specified cells; i.e., the MCNPX-PoliMi collision log permits perfect particle identification (PID). Using perfect PID in TCPH analysis, however, would miscalculate experiment results by overestimating the neutron and gamma detection rates. This overestimation is shown in Figure 4.3 for the bare BeRP ball particle spectra.

<div style="text-align:center">(a)   (b)</div>
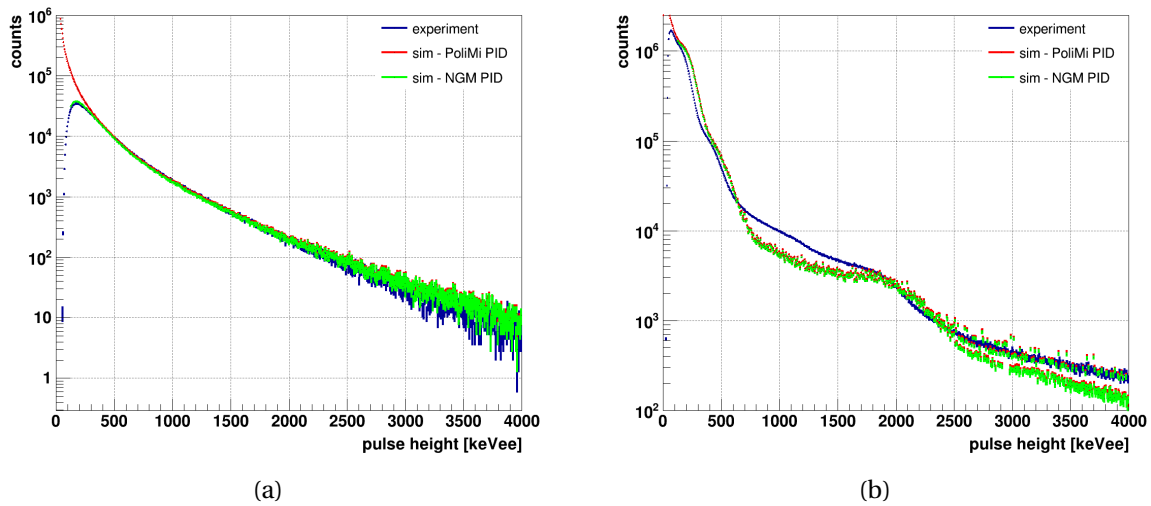
Figure 4.3 Particle identification effect. The (a) neutron and (b) gamma spectra for the bare BeRP ball (blue) experiment, (red) simulation using MCNPX-PoliMi PID, and (green) simulation using NCAI-style PID show the overestimation of the events at low energies when MCNPX-PoliMi PID is used.

Only a portion of recorded events are used when applying TCPH analysis to measurement data by conducting PID as described in Section 3.2. This reduction is due to classifying particles as being within two standard deviations of a PSD parameter mean, and for neutrons more than five standard deviations away from the gamma PSD parameter mean. A similar method of PID was implemented in simulation analysis. The particle type identified by MCNPX-PoliMi and light output were used to

www.manaraa.com

randomly sample a PSD parameter from the appropriate NCAI PSD parameter distribution (gamma or neutron) shown in Figure 2.15. The number of standard deviations away from each particle type mean was then determined and recorded. In this manner, the same particle type parameters used in analyzing the DAF experiments were used in the simulation.

The neutron spectra shown in Figure 4.3(a) illustrates the effect of such an implementation. The low energy drop-off in the blue and green curves, representing measurement and simulation using NCAI-style PID respectively, is due to the cut requiring a neutron to be at least $5\sigma_\gamma$ away from the gamma PSD mean $\overline{p}_\gamma$.

The gamma spectra, shown in Figure 4.3(b), do not exhibit the same behavior. The underestimation of the simulation gammas in the 700-1900 keVee range may be attributed to inaccurate initial conditions used in solving the Bateman equations. The low energy drop-off in the experiment spectrum is due to hardware threshold effects, and cannot be replicated by implementing NCAI-style PID methods. Instead, a light output threshold of 125 keVee was implemented. This threshold was chosen because it replicates the threshold used in analysis of the DAF measurements. The energy threshold used in the measurement analysis was set to eliminate the area of the PSD parameter vs. pulse height histogram with the most overlap and such that only 1 MeV or more energetic neutrons would be counted.

Simulation PID was therefore conducted using the same parameters and methodology as the experiment. This implementation, however, does not completely replicate the particle misidentification or detection efficiency of the NCAI system. A more detailed comparison between experiment and simulation follows.

4.2   Comparison with Experiment

To benchmark the MCNPX-PoliMi model, simulations were performed to replicate the scene 2 (^{252}Cf only) and scene 3 (BeRP only) DAF measurements. The degree to which the simulations correctly

replicated the measurements was determined by comparing the neutron energy spectra and gross count rates, as well as the apparent time-of-flight histograms, for these scenes. The neutron spectra in Figure 4.4 show good agreement, and the gross neutron count rates differed by under 2% for both scenes.
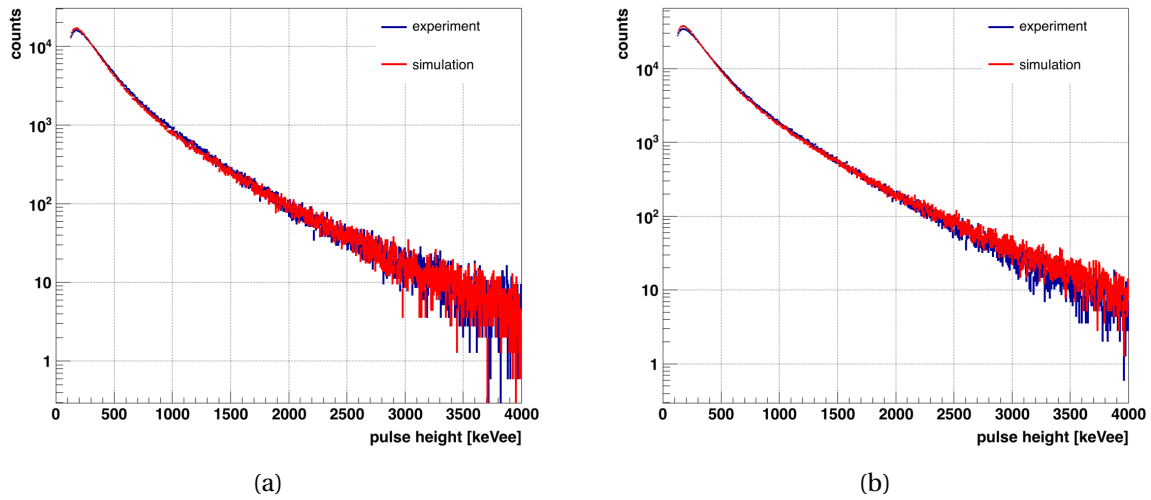
Figure 4.4 Neutron spectra comparison. The (a) scene 2 and (b) 3 three neutron energy spectra for (blue) experiment and (red) simulation.

Figure 4.5 shows the apparent time-of-flight histograms for scenes 2 and 3. The true coincidence rates were determined by subtracting the accidental contribution to the time interval analysis histograms, as described in Section 3.2. These histograms show modest agreement, with chi-squared values of 7.8 and 22.1 for scenes 2 and 3, respectively, in the time interval $(0 < \Delta t < 500)$ ns. The chi-squared value was calculated by

$$\chi^2 = \frac{1}{N_b} \sum_{b}^{N_b} \frac{(M_b - S_b)^2}{\sigma_{M_b}^2},$$

(4.1)

65

where N_b is the number of histogram bins in the apparent time-of-flight interval, M_b and S_b are the counts in the bin b for the measurement and simulation histograms respectively, and $\sigma^2_{M_b}$ is the variance in the measurement histogram bin.

The peak in the interval $(0 < \Delta t < 25)$ ns is due to inelastic scatter near the detector or gamma misclassification. Eliminating that peak reduces the chi-squared values to 5.8 and 5.9, which corresponds to a root-mean-square difference of about 2.4 standard deviations. The peak in the interval $(0 < \Delta t < 25)$ ns is explained further in Section 4.4. The differences between the histograms in the interval $(25 < \Delta t < 100)$ ns may be attributed to errors in the recorded source-mask and mask-detector distances.
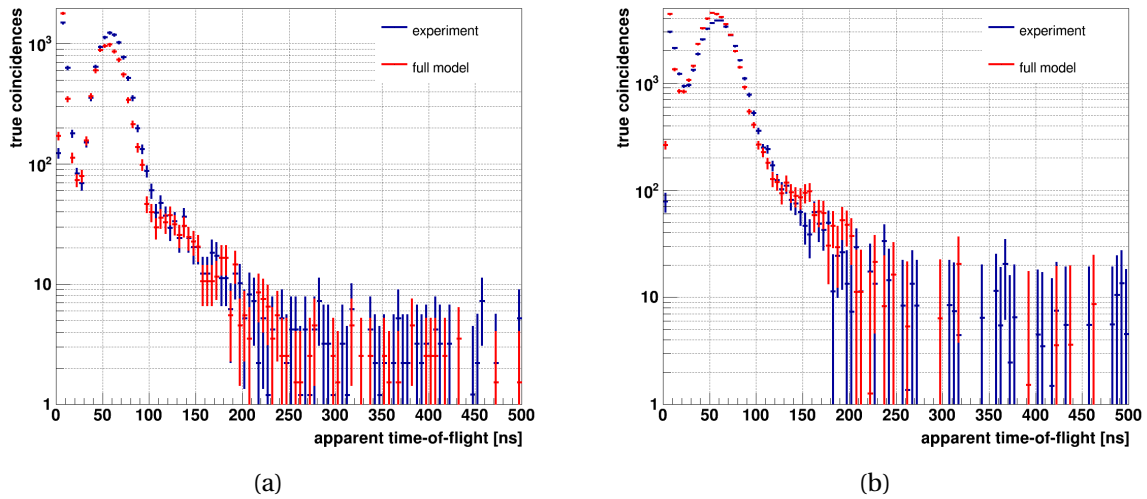
Figure 4.5 Apparent time-of-flight comparison. The (a) scene 2 and (b) scene 3 apparent time-of-flight for (blue) experiment and (red) simulation.

The models are suitable for the present work because their use produces conservative results when applying TCPH analysis. The measurement and simulation ROI counts in the reals (fission chain reaction neutron) images for scene 2 and scene 3 are shown in Table 4.2.

Table 4.2 TCPH analysis results comparison for scene 2 and scene 3 measurement and simulation. The ROI counts in the reals (fission chain reaction neutrons) image for the scene 2 and scene 3 measurements are compared with simulation. The last column indicates the statistical significance N/σ of the source presence above background in the final image.

Scene	Experiment	Reals	N/σ
2	Measurement	-67 ± 92	-0.7
	Simulation	-88 ± 68	-1.3
3	Measurement	$2,060 \pm 324$	6.4
	Simulation	$1,715 \pm 298$	5.8

4.3   Lower Limit of TCPH Applicability

Chapter 3 showed that applying TCPH analysis to a measurement performed with the NCAI would eliminate a non-multiplying assembly from a fast neutron image while retaining a multiplying assembly. Additionally, it was shown that a multiplying assembly would remain in a fission chain reaction neutron image in a single source scene. This section explores the limits of TCPH analysis by estimating the minimum multiplication necessary to preserve a multiplying source in a fission chain reaction neutron image. Both solid and hollow spherical WGPu assemblies were modeled.

4.3.1   Solid WGPu Sphere

These simulations modeled a solid sphere of WGPu metal with the same composition and density as the BeRP ball for the multiplying assembly. Each simulation is equivalent to a one hour measurement. The radius of the sphere was varied to change the multiplication of the assembly and the multiplication factor was estimated using MCNPX. The results of these simulations, shown in Figure 4.6, indicate a solid assembly must have a multiplication of at least 3.0 to be preserved at a 1σ level in a fission chain reaction neutron image formed from a one hour measurement; the lower limit is at least 3.2 at a 2σ level.

Radius [cm]	Mass [kg]	Multiplication	ROI Counts
3.7983	4.483	4.454 ± 0.011	$1,715 \pm 298$
3.6526	4.000	3.985 ± 0.009	932 ± 219
3.4268	3.304	3.411 ± 0.006	250 ± 129
3.3402	3.060	3.215 ± 0.005	145 ± 68
3.2335	2.776	3.032 ± 0.004	59 ± 57
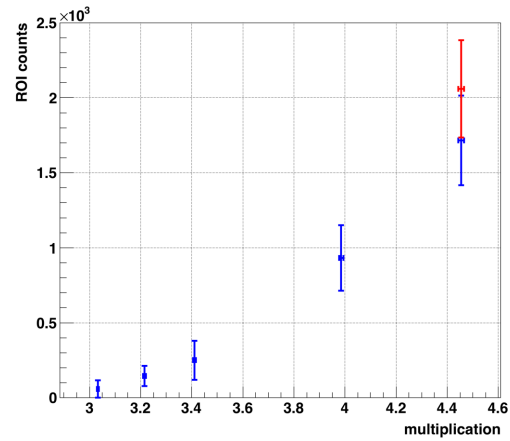
Figure 4.6 Solid WGPu sphere ROI counts vs. multiplication. The table and plot show the results of varying the outer radius of a solid sphere of WGPu. The ROI counts are from the chain reaction neutrons image and the red data point in the plot represents the DAF measurement of the BeRP ball.

4.3.2 Hollow WGPu Sphere

These simulations again used a sphere of WGPu metal with the same composition and density as the BeRP ball. Each simulation is equivalent to a one hour measurement. The multiplication of the WGPu was changed by holding the outer radius of the sphere fixed at 3.7983 cm and varying the radius of a central cavity. Changing the multiplication in this manner kept the gamma detection rate roughly constant, as the gamma emission rate is proportional to the sphere surface area. By keeping the gamma emission rate the same but changing the multiplication, multiplication was isolated as an independent variable in this series of simulations[3]. The results of these simulations, shown in Figure 4.7, indicate a hollow assembly must have a multiplication of at least 2.7 to be preserved at a 1σ level in a fission chain reaction neutron image formed from a one hour measurement; the lower limit is at least 3.0 at a 2σ level.

The results in Table 4.6 and Table 4.7 may also be used to infer an assembly is hollow when

---

[3]In contrast, changing the radius of the solid sphere of WGPu changed the multiplication and gamma emission rate simultaneously.

| Inner Radius [cm]	Mass [kg]	Multiplication	ROI Counts
N/A	4.483	4.454 ± 0.011	$1,715 \pm 298$
1.00	4.401	4.014 ± 0.008	$1,078 \pm 235$
1.25	4.323	3.738 ± 0.007	649 ± 210
1.50	4.206	3.417 ± 0.005	280 ± 159
1.75	4.043	3.080 ± 0.004	173 ± 82
2.00	3.827	2.748 ± 0.003	78 ± 71
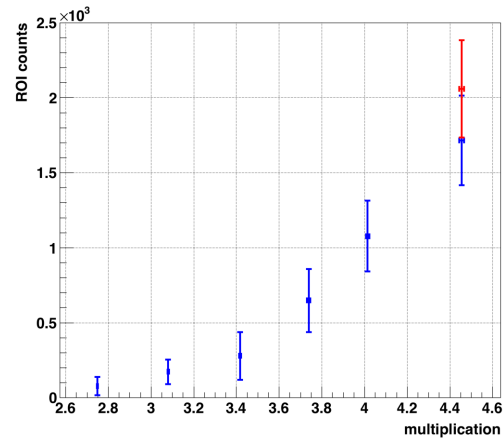
Figure 4.7 Hollow WGPu sphere ROI counts vs. multiplication. The table and plot show the results of varying the inner radius of a sphere of WGPu with a central cavity. The ROI counts are from the chain reaction neutrons image and the red data point in the plot represents the DAF measurement of the BeRP ball.

paired with other information. For example, a gamma spectrum analysis of a 3.5 cm sphere may identify it as containing WGPu. However, this analysis provides no information about the interior of the sphere because the mean free path of plutonium and americium gammas in plutonium metal is less than a centimeter. Should the source be eliminated from the fission chain reaction neutron image, one could conclude that the interior is hollow.

The multiplication threshold estimates presented may be lowered by increasing the contrast in the chain reaction neutron images. This possibility is investigated in the next section.

4.4 The Effect of Neutron Scatter Events

Neutron scatter events have the potential to impact the results of TCPH analysis, as discussed in Section 2.5. This section identifies the source and impact of scattered neutrons in the model previously described, and then explores two extreme cases. The first case involved deliberately introducing scattering materials in the scene 2 geometry, while the second involved removing scattering materials in the scene 3 geometry.

69

4.4.1 Source and Impact of Scattered Neutrons

Figure 4.8 shows excess time histograms, each equivalent to a two hour measurement of a 23 μCi ^{252}Cf source. The simulations were performed with different model geometries to identity the source and impact of scattered neutrons. The blue data points represent a simulation using the full model of the NCAI, as shown in Figure 4.1. The red data points are from the same model, but with the floor removed. Finally, the green data points are from a simulation using a minimal model, consisting only of the ^{252}Cf source, mask, and block detectors; i.e., all the structural components of the NCAI have been removed in addition to the floor.
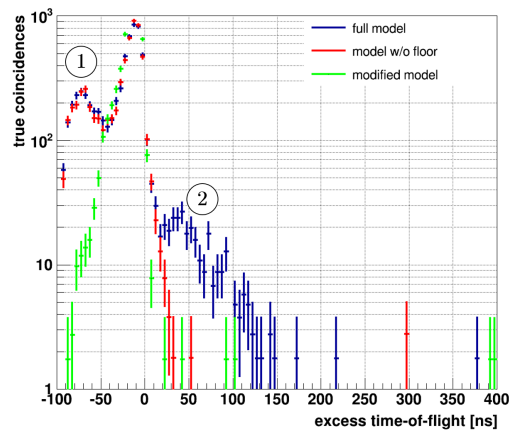
Figure 4.8 Identifying the source of neutron scatter. The excess time histograms for the (blue) full model, (red) full model without the floor, and (green) minimal model containing only the source, mask, and block detectors for a simulation of the ^{252}Cf source illustrate the primary sources of scattered neutrons. The peak in the histogram of the full model simulation in region (1) is due to inelastic scatter near the detector. The width of the distribution in the histogram of the full model simulation in region (2) is due to floor scatter.

Examination of these histograms shows two sources of neutron scatter events. The peak in the histogram of the full model simulation in the interval $(-100 < \Delta t_{ex} < -50)$ ns can be attributed to inelastic scatter events near the detector. This peak is labeled (1) in Figure 4.8. In these events, the

gamma produced in the inelastic scatter is detected in coincidence with a neutron; the neutron appears to have arrived early because the gamma is produced close to the detector. This effect will not cause the misclassification of a non-multiplying assembly because it moves events to the left in the time analysis histograms.

On the other hand, scatter events that cause the neutron to appear later than it would otherwise do have the potential to lead to misclassification of a non-multiplying assembly. For a non-multiplying source such as ^{252}Cf in an ideal measurement, no events should appear to the right of $\Delta t_{ex} = 0$ since the excess time is measured relative to a single fission event. Scatter events, particularly by heavy nuclei where a minimal amount of kinetic energy is lost, can cause neutrons to appear late and be misclassified as fission chain reaction neutrons. The width of the distribution in the histogram of the full model simulation in the interval $(15 < \Delta t_{ex} < 150)$ ns can be attributed to neutrons scattered by the floor. This region is labeled (2) in Figure 4.8.

4.4.2   Increasing Neutron Scatter Events

Floor scatter events are outside the detector field-of-view, so they are eliminated from images by subtracting mask and anti-mask measurements. However, any scatter events within the detector field-of-view causing neutrons to appear late would be retained; the accumulation of many such late arriving neutrons could confound the TCPH analysis of a non-multiplying assembly.

To examine this possibility, the scene 2 geometry was modified by placing the ^{252}Cf source inside a scattering assembly. The assembly was a 9.6 cm diameter sphere of lead with a 2 cm diameter central hollow cavity. Additionally, the sphere had a conical void with an approximately 22 degree opening angle oriented toward the NCAI mask. Lead was chosen because incident neutrons lose on average only 1% of their energy per scatter with a lead nucleus; i.e., they can scatter enough to appear late but not down-scatter below the detection energy threshold. The void portions of the sphere were included and oriented toward the mask so as to not shield the detector from the gammas. This assembly is shown in Figure 4.9.

71
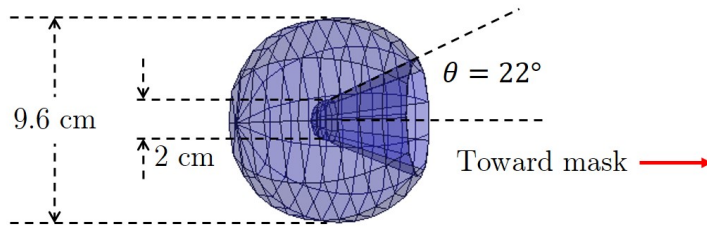
Figure 4.9 ^{252}Cf source scattering assembly. In this modification to the scene 2 geometry, the ^{252}Cf source was placed in a 9.6 cm diameter sphere of lead with a 2 cm diameter central cavity and 22 degree conical opening oriented toward the NCAI mask.

The resulting excess time histogram from using this modified model is shown in Figure 4.10, where it is compared to the scene 2 measurement and full model simulation. These histograms share similar features. However, a portion of the modified model distribution is due to scatters inside the detector field-of-view and these events are therefore retained in the TCPH-filtered image. A comparison of the TCPH-filtered, accidentals, and fission chain reaction neutrons image ROIs for the measurement and two simulations are shown in Table 4.3. The ^{252}Cf source is retained in the fission chain reaction neutron image at a 1.1σ level with the presence of the scattering sphere.

Table 4.3 ROI count comparison for images formed using different models. The ROI counts for the full model and model with the floor removed are compared for the TCPH-filtered, accidentals, and reals (fission chain reaction neutrons) images. The last column indicates the statistical significance N/σ of the source presence above background in the final image.

Model	TCPH-Filtered	Accidentals	Final	N/σ
Experiment	188 ± 92	255 ± 5	-67 ± 92	-0.7
Full	106 ± 68	194 ± 5	-88 ± 68	-1.3
Modified	322 ± 88	234 ± 5	88 ± 81	1.1

The scattering assembly in the modified model is a deliberate "spoof." Although the modified model simulation indicates that neutron scattering inside the detector field-of-view has the potential to lead to an assembly being misclassified as multiplying, the source was not identified as a

72
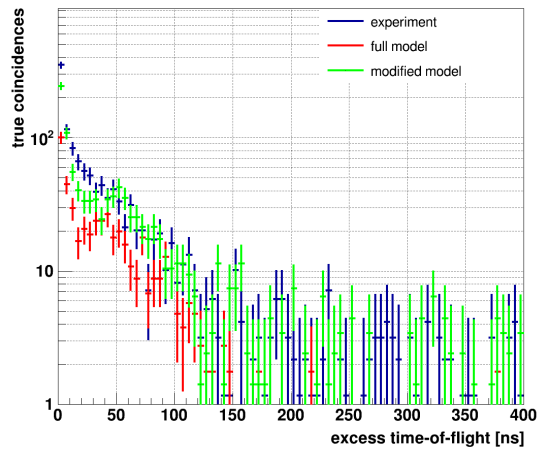
Figure 4.10 Excess time histograms comparison for different models. The (blue) scene 2 measurement, (red) scene 2 model, and (green) modified model with scattering assembly excess time histograms share similar features, but the modified model distribution contains scatter events from within the detector field-of-view.

multiplying assembly when the conical void faced away from the NCAI mask. A host would have to control the orientation of the inspection object relative to the imager in order to successfully spoof the measurement using this scattering assembly.

4.4.3   Reducing Neutron Scatter Events

The scene 3 model was used to investigate the possibility of increasing the source contrast in the fission chain reaction neutrons image by reducing albedo neutrons. The reduction in albedo neutrons was accomplished by removing the floor from the scene 3 model. Simulation with and without the floor showed the reduction of albedo neutrons has two effects that increase the contrast of a fast neutron image.

The first effect is a reduction in the uncertainty associated with the source ROI in the TCPH-filtered image. This uncertainty is directly proportional to the square root of the total counts in the detector that are used to form the image, as discussed in Section 2.8. Albedo neutrons contribute to

73

the total count, but are eliminated when using mask and anti-mask data sets; i.e., the estimated source counts within a region of interest is the same with and without albedo neutrons. However, the contrast of the image increases with a reduction in albedo neutrons by lowering the ROI uncertainty.

This effect is illustrated by the images constructed by TCPH-filtered neutron events shown in Figure 4.11. In these simulations, approximately 22% fewer neutrons were detected in the TCPH excess time interval for the model with the floor removed. This reduction, attributed to the absence of albedo neutrons, in neutron counts resulted in decrease of 12% in ROI uncertainty, while the difference in ROI counts is under 1%.

(a)   (b)
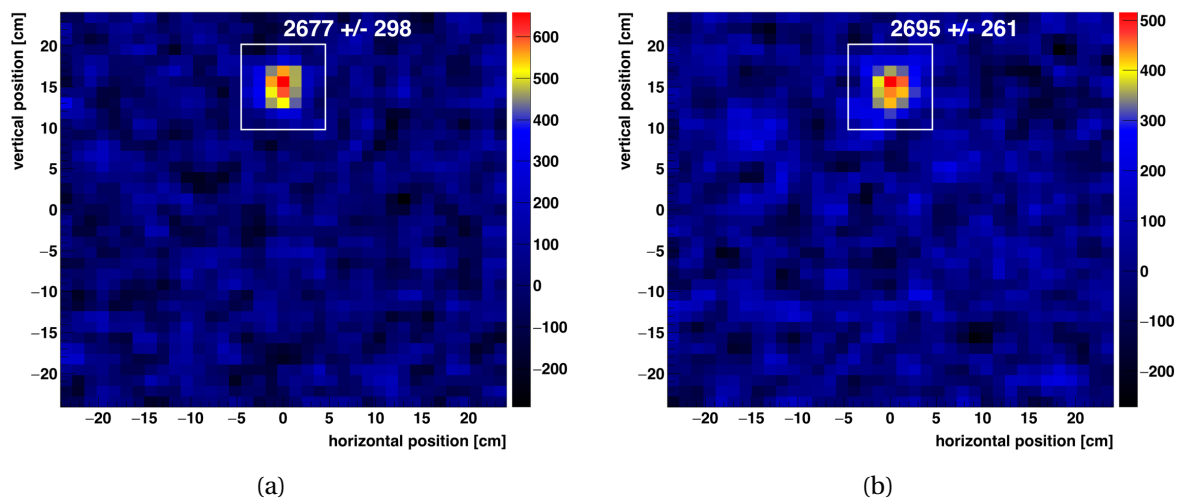
Figure 4.11 Reduction of total neutron events. The (a) full model and (b) model with the floor removed TCPH-filtered images show a 12% reduction in ROI uncertainty due to a reduction in total neutron events in the model with the floor removed.

The second effect is an increase the ROI counts in the fission chain reaction neutron image. Albedo neutrons widen the excess time distribution, causing the point at which the FAR^4 falls below the threshold of 2.5 to increase. This increase, shown in Figure 4.12, is approximately 15 ns for the

[4]The fission chain reaction-to-accidental ratio FAR is described in Section 3.2.

full model. However, the counts in the excess time distribution of the full model above that of the model with the floor removed do not contribute to the TCPH-filtered image because they come from outside the detector field-of-view. Instead, the wider excess time interval used in the TCPH filter leads to a larger accidentals scaling factor. A larger accidental contribution is therefore subtracted from the TCPH-filtered ROI, resulting in a lower ROI count for the fission chain reaction neutron image. A summary of these results is presented in Table 4.4.
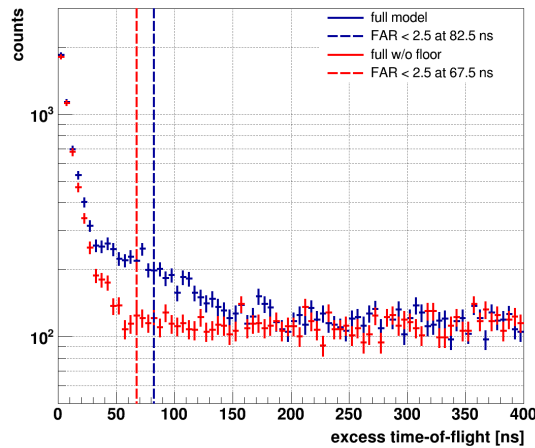
Figure 4.12 Widening the excess time distribution. The excess time histograms for the (blue) full model and (red) model with the floor removed show the distribution widens with the inclusion of albedo neutrons. The dashed lines represent when the FAR < 2.5.

Table 4.4 ROI count comparison for images formed using different models. The full model and model with the floor removed ROI counts are compared for the TCPH-filtered, accidentals, and reals (fission chain reaction neutrons) images. The last column indicates the statistical significance N/σ of the source presence above background in the reals image.

Model	TCPH-Filtered	Accidentals	Reals	N/σ
Full	$2,677 \pm 298$	962 ± 6	$1,715 \pm 298$	5.8
No Floor	$2,695 \pm 261$	784 ± 5	$1,911 \pm 261$	7.3

These results indicate an increase in source contrast in the fission chain reaction neutrons image is possible through a reduction in albedo neutrons. The effect was further demonstrated by modifying the scene 3 (BeRP only) model to include a barrier to reduce floor scatter. This barrier, shown in Figure 4.13, was made of two slabs of borated polyethylene. The first slab measured 96 in × 48 in × 6 in and was placed horizontally underneath the source on the floor. The second slab measured 96 in × 18.5 in × 6 in and was placed vertically at the base of the mask assembly.
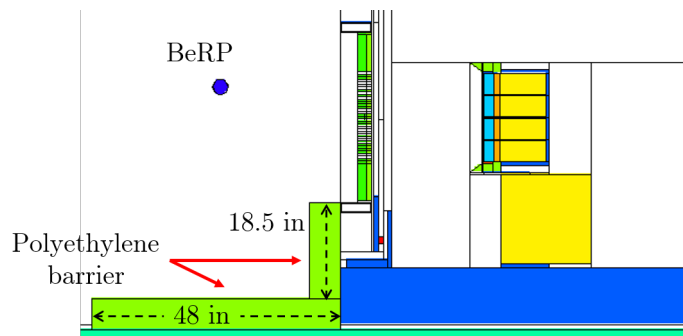
Figure 4.13 Modified scene 3 model with borated polyethylene barrier. Each slab was 6 inches thick and 96 inches wide.

The results of the simulation including the borated polyethylene barrier, shown in Table 4.5, further demonstrate an increase in source contrast in the fission chain reaction neutron image due to a decrease in albedo neutrons. The addition of the borated polyethylene barrier significantly reduced floor albedo. The increase in contrast may be exploited to reduce the multiplication threshold for which TCPH analysis is successful in preserving a multiplying assembly in a fission chain reaction neutron image.

Table 4.5 ROI count comparison for images formed using different models. The full, no floor, and polyethylene barrier model ROI counts are compared for the TCPH-filtered, accidentals, and reals (fission chain reaction neutrons) images. The last column indicates the statistical significance N/σ of the source presence above background in the reals image.

Model	TCPH-Filtered	Accidentals	Reals	N/σ
Full	$2,677 \pm 298$	962 ± 6	$1,715 \pm 298$	5.8
No Floor	$2,695 \pm 261$	784 ± 5	$1,911 \pm 261$	7.3
Poly Barrier	$2,600 \pm 259$	790 ± 5	$1,810 \pm 259$	7.0

4.5 Simulation Summary

Simulations were performed using MCNPX-PoliMi to investigate the multiplication limit of TCPH analysis and the effect of neutron scatter. The models used combined fission and decay gamma sources; the inclusion of the gamma source was found to be necessary to prevent an underestimation of the accidental coincidence rate. These models were benchmarked against the scene 2 (^{252}Cf only) and scene 3 (BeRP only) measurements, and found to agree in terms of neutron spectra, gross count rate, and apparent time-of-flight. The differences noted between the models and experiments make the simulations conservative.

A spherical WGPu source was used to estimate the lower limit of multiplication an assembly must have in order to remain in a fission chain reaction neutron image. These simulations were performed for both solid and hollow spheres. The multiplication of the solid sphere was changed by varying the radius, while the multiplication of the hollow sphere was changed by varying the radius of a central cavity and holding the outer radius fixed. The lower limit for a solid sphere was found to be $M \simeq 3.0$, while a hollow sphere was found to be $M \simeq 2.7$. These limits are estimates for a one hour measurement with a 1σ source presence threshold in the fission chain reaction neutron image.

A series of simulations using modified scene 2 and 3 models was performed to identify the source and impact of scattered neutrons. Simulations using a ^{252}Cf source in the scene 2 geometry, modified to remove the floor and again to include only the source, mask, and block detectors, showed that

77

floor scatter is the primary source of albedo neutrons. The scene 2 geometry was again modified to include a scattering assembly around the ^{252}Cf source; this simulation demonstrated the possibility of misclassifying a non-multiplying source as multiplying.

Finally the scene 3 model was modified to remove the floor and again to include a borated polyethylene albedo barrier. Simulations with these models showed that reducing floor scatter increases the contrast of a source in a fission chain reaction neutron image. The increase in the statistical significance of the source ROI in the fission chain reaction neutron image is attributed to an increase in the reals count N and a decrease in the uncertainty σ.

CHAPTER

5

CONCLUSIONS AND FUTURE WORK

5.1 Conclusions

The work presented demonstrated it is possible to distinguish between multiplying and non-multiplying assemblies in fast neutron images. This ability to classify sources was proven through measurement of the BeRP ball (multiplying) and ^{252}Cf (non-multiplying) sources, separately and together. In each measurement, the effect of applying TCPH analysis was quantified with uncertainty.

It is significant that one of the measurements included a multiplying and non-multiplying source in the same scene, and that the ^{252}Cf was removed while the BeRP ball was retained in the fission chain reaction neutron image. The ability to classify multiple sources in the same scene is new and was made possible by the imaging capability of the NCAI combined with TCPH analysis.

It is also significant that TCPH analysis was successful for both sources when imaged separately; i.e, the BeRP ball was retained and the ^{252}Cf source was eliminated. The analysis of these measurements demonstrated the success of applying the method to the measurement of both sources was not merely due to a difference in source intensities.

It was shown that a solid sphere of WGPu metal must have a neutron multiplication of $M \simeq 3.0$ in order to be preserved at a 1σ level in an image after applying TCPH analysis; for a hollow sphere of WGPu metal, this limit is $M \simeq 2.7$. This difference, when paired with other information such as the isotopic composition and diameter of the source, could allow an observer to infer that the source is hollow.

Simulations also demonstrated the effect of neutron scatter on TCPH analysis. A deliberate spoof device showed that an increase in neutron scatter within the detector field-of-view introduces the possibility of misclassifying a non-multiplying source as multiplying when the host controls the source-detector orientation. On the other hand, it was shown that a decrease in neutron scatter outside the detector field-of-view led to a modest increase in source contrast in the fission chain reaction neutron image. In both cases, the results indicate the reduction of neutron scatter has a positive effect on TCPH analysis results.

5.2   Future Work

This work demonstrated the ability to classify fast neutron sources as multiplying (or not) by applying TCPH analysis to measurements made with the NCAI. However, there are several areas in which the process may be refined.

5.2.1   Fission Chain Reaction Neutrons

The key component in the application of TCPH analysis is the detection of fission chain reaction neutrons by estimating energy deposition and comparing it to the apparent kinetic energy. The

estimation of apparent kinetic energy is, in turn, based on estimating the time of fission and the distance measurement from the source to the detector.

This work used the furthest distance from the center of the source to the rear of the imaging plane as the source-detector distance. This choice was deliberately conservative; i.e., it had the effect of moving the discrimination line to the right on the TCPH histogram, thereby reducing the number of events classified as fission chain reaction neutrons. The efficiency of detecting true fission chain reaction neutrons would increase by using the pixel coordinates to estimate the true distance from the source.

The efficiency of detecting fission chain reaction neutrons may also be increased by increasing the gamma detection efficiency. An increase in gamma detection efficiency could be accomplished by placing additional gamma detectors near the source and conducting measurements in coincidence with the NCAI.

5.2.2 TCPH Filter Interval

The fission chain reaction-to-accidental coincidence ratio was used to determine the upper limit of the TCPH filter. This ratio was calculated using all neutron events, including neutrons not modulated by the mask. A similar ratio calculated using only neutrons modulated by the mask would eliminate the overestimation of the accidental coincidence scaling factor noted in the investigation of albedo neutrons. The ideal ratio would be calculated based on a source-by-source basis dependent on location in the object plane.

5.2.3 Significance of Simulation Results

The results for each model simulated in this work represent one trial of a one hour measurement. Performing multiple trials for each model could improve the estimates of the mean ROI counts and uncertainty in the fast neutron images, and these estimates would provide insight into the significance of the simulation results.

81

For example, the increase in source contrast observed when reducing floor scatter was based in part on a reduction in the uncertainty of the source ROI in the TCPH-filtered image. However, the uncertainty of that uncertainty is unknown. Performing a series of simulations using the model with the polyethylene albedo barrier would allow the uncertainty of the source ROI uncertainty to be calculated. This calculation would indicate whether the reduction in source ROI uncertainty corresponding to the reduction in floor scatter was significant.

5.2.4 Low Multiplication Sources

The measurements conducted in support of this work used a highly multiplying source; the BeRP ball has a neutron multiplication $M = 4.5$. Although estimates of the lower limit of multiplication for which TCPH analysis of fast neutron images were made through simulation, measurements of low multiplication sources would be valuable. Additional measurements would facilitate the refinement of methods developed for detecting fission chain reaction neutrons and creating a TCPH filter.

The purpose of this work is to develop a methodology that classifies a neutron source as multiplying in a scene that may include inhomogeneous, extended, or multiple sources. The continued improvement of this method could make it a valuable part of a larger nuclear warhead verification methodology, as it confirms a necessary attribute of a nuclear weapon.

BIBLIOGRAPHY

[1]   Avens, L. R. et al. "The Fissile Material Transparency Technology Demonstration". *LA-UR-01-3570, Los Alamos National Laboratory* (2001).

[2]   Brubaker, E. *Email*. Personal correspondence, 2016.

[3]   Cannon, T. M. & Fenimore, E. E. "Coded aperture imaging: many holes make light work". *Optical Engineering* **19**.3 (1980), pp. 283–289.

[4]   Chadwick, M. B. et al. "ENDF/B-VII.1 nuclear data for science and technology: Cross sections, covariances, fission product yields and decay data". *Nuclear Data Sheets* **112**.12 (2011), pp. 2887–2996.

[5]   *Chart of Nuclides*. http://www.nndc.bnl.gov/nudat2/. Accessed: 2017-04-09.

[6]   Cifarelli, D. M. & Hage, W. "Models for a three-parameter analysis of neutron signal correlation measurements for fissile material assay". *Nuclear Instruments and Methods in Physics Research, Section A: Accelerators, Spectrometers, Detectors and Associated Equipment* **251**.3 (1986), pp. 550–563.

[7]   Duderstadt, J. & Hamilton, L. *Nuclear Reactor Analysis*. New York: John Wiley & Sons, Inc., 1976.

[8]   Enqvist, A. et al. "A combined neutron and gamma-ray multiplicity counter based on liquid scintillation detectors". *Nuclear Instruments and Methods in Physics Research, Section A: Accelerators, Spectrometers, Detectors and Associated Equipment* **652**.1 (2011), pp. 48–51.

[9]   Ensslin, N. et al. "Application Guide to Multiplicity Counting". *LA-13422-M, Los Alamos National Laboratory* (1998).

[10] Fenimore, E. E. & Cannon, T. M. "Coded aperture imaging with uniformly redundant arrays". *Applied Optics* **17**.3 (1978), pp. 337–347.

[11] Fleenor, M. C. et al. "Correlated statistical uncertainties in coded-aperture imaging". *Nuclear Instruments and Methods in Physics Research, Section A: Accelerators, Spectrometers, Detectors and Associated Equipment* **784** (2015), pp. 370–376.

[12] Fuller, J. "Verification on the road to zero: issues for nuclear warhead dismantlement". *Arms Control Today* **40**.10 (2010), pp. 19–27.

[13] *GEM Series Coaxial HPGe Detector Product Configuration Guide*. http://astro1.panet.utoledo.edu/~relling2/teach/4780/Ortec_HPGe_Germanium_GEM_Detectors.pdf. Accessed: 2017-04-13.

[14] Glasstone, S. & Dolan, P. J. *The Effects of Nuclear Weapons*. Third. United States Department of Defense and Department of Energy, 1977.

[15] Hall, J. M. et al. "The Nuclear Car Wash: Neutron interrogation of cargo containers to detect hidden SNM". *Nuclear Instruments and Methods in Physics Research, Section B: Beam Interactions with Materials and Atoms* **261** (2007).

[16] Hamel, M. et al. "2015 Experimental Campaign at the Device Assembly Facility". University and Industry Technical Interchange Review Meeting, 8 Jun 2016, Raleigh, NC.

[17] Hausladen, P. & Newby, J. *Passive and Active Thermal and Fast-Neutron Imaging Measurements and Coincidence-Gated Imaging of SNM Inspection Objects*. Tech. rep. Oak Ridge National Laboratory, 2015.

[18] Hausladen, P. et al. "Fast-Neutron Coded-Aperture Imaging of Special Nuclear Material Configurations". *Institute of Nuclear Materials Management 53rd Annual Meeting* (2012).

[19] Hausladen, P. et al. *Active Fast-Neutron Imaging Measurements of Inspection Objects at the INL ZPPR Facility*. Tech. rep. Oak Ridge National Laboratory, Idaho National Laboratory, 2014.

[20] Hollas, C. L. et al. "Determination of neutron multiplication of subcritical HEU systems using delayed neutrons". *Nuclear Instruments and Methods in Physics Research, Section A: Accelerators, Spectrometers, Detectors and Associated Equipment* **543**.2-3 (2005), pp. 559–569.

[21] Knoll, G. F. *Radiation Detection and Measurement*. Third. New York: John Wiley & Sons, Ltd, 2000.

[22] Krane, K. S. *Introductory Nuclear Physics*. New York: John Wiley & Sons, Inc., 1988.

[23] Kristensen, H. M. & Norris, R. S. *Status of World Nuclear Forces*. `http://fas.org/issues/nuclear-weapons/status-world-nuclear-forces/`. Accessed: 2017-02-09.

[24] Lawrence, C. C. et al. "Neutron response characterization for an EJ299-33 plastic scintillation detector". *Nuclear Instruments and Methods in Physics Research, Section A: Accelerators, Spectrometers, Detectors and Associated Equipment* **759** (2014), pp. 16–22.

[25] Lewis, E. E. *Fundamentals of Nuclear Reactor Physics*. Brulington, MA: Academic Press, 2008, p. 280.

[26] Luke, S. J. & Archer, D. E. "Gamma Attribute Measurements - Pu-300, Pu600, Pu900". *41st Annual Meeting of the Institute of Nuclear Materials Management*. 2000, pp. 1–13.

[27]   Marleau, P. et al. "Gamma/Neutron Time-Correlation for Special Nuclear Material Detection - Active Stimulation of Highly Enriched Uranium". *SAND2013-7442, Sandia National Laboratories* (2013).

[28]   Mascarenhas, N. et al. "Development of a Neutron Scatter Camera for Fission Neutrons". *2006 IEEE Nuclear Science Symposium Conference Record* **2**.2 (2006), pp. 185–188.

[29]   Mattingly, J. "Polyethylene-Reflected Plutonium Metal Sphere: Subcritical Neutron and Gamma Measurements". *SAND2009-5804-R3, Sandia National Laboratories* (2009).

[30]   Mattingly, J. et al. "CNEC and CVT Subcritical Experiments with Category I Special Nuclear Material at the Nevada National Security Site Device Assembly Facility". *Proceedings of INMM 57th Annual Meeting* (2016).

[31]   Miller, E. C. "Characterization of Fissionable Material using a Time-Correlated Pulse-Height Technique for Liquid Scintillators". PhD. University of Michigan, 2012.

[32]   Miller, E. C. et al. "Time-correlated pulse-height measurements of low-multiplying nuclear materials". *Nuclear Instruments and Methods in Physics Research, Section A: Accelerators, Spectrometers, Detectors and Associated Equipment* **729** (2013), pp. 108–116.

[33]   Monterial, M. et al. "Time-Correlated-Pulse-Height Technique Measurements of Fissile Samples at the Device Assembly Facility". *Institute of Nuclear Materials Management Annual Meeting*. 2013.

[34]   Mueller, J. & Mattingly, J. "Neutron and Gamma Ray Coincidence Measurements of a High-Multiplication, Subcritical Assembly of Weapons-Grade Plutonium". *IEEE Nuclear Science Symposium Conference Record*. 2015.

[35]   Nakae, L. F. et al. "Recent Developments in Neutron Detection and Multiplicity Counting with Liquid Scintillator". *LLNL-CONF-422505, Lawrence Livermore National Laboratory* (2010).

[36]   *New START*. https://www.state.gov/t/avc/newstart/. Accessed: 2017-02-09.

[37]   Newby, J. *Placeholder for docueting NGM*. *** properly document NGM ***. 2014.

[38]   Newby, J. et al. "Performance of Fast-Neutron Imaging Detectors Based on Plastic Scintillator". *ORNL/TM-2013/82, Oak Ridge National Laboratory* (2013).

[39]   Padovani, E. et al. *MCNPX-PoliMi Users Manual*.

[40]   Paff, M. G. et al. "Gamma/neutron time-correlation for special nuclear material detection - Active stimulation of highly enriched uranium". *Annals of Nuclear Energy* **72** (2014), pp. 358–366.

[41]   Pelowitz, D. B., ed. *MCNPX User's Manual*. 2011.

[42]   Poitrasson-Rivière, A. et al. "Angular-resolution and material-characterization measurements for a dual-particle imaging system with mixed-oxide fuel". *Nuclear Instruments and Methods in Physics Research, Section A: Accelerators, Spectrometers, Detectors and Associated Equipment* (2015).

[43]   Reif, K. *New START at a Glance*. https://www.armscontrol.org/factsheets/NewSTART. Accessed: 2017-02-11.

[44]   Reilly, D. et al. *Passive Nondestructive Assay of Nuclear Materials*. Ed. by Kreiner, S. NUREG/CR-5550, LA-UR-90-732, Los Alamos National Laboratory, 1991.

[45]   Robba, A. A. et al. "Neutron multiplication measurements using moments of the neutron counting distribution". *Nuclear Instruments and Methods In Physics Research* **215**.3 (1983), pp. 473–479.

[46]   Romero, R. "Application Guide to Shufflers". *LA-13819-MS, Los Alamos National Laboratory* (2001).

[47]   Runkle, R. C. et al. "Rattling nucleons: New developments in active interrogation of special nuclear material". *Nuclear Instruments and Methods in Physics Research, Section A: Accelerators, Spectrometers, Detectors and Associated Equipment* **663**.1 (2012), pp. 75–95.

[48]   Terrell, J. "Distributions of fission neutron numbers". *Physical Review* **108**.3 (1957), pp. 783–789.

[49]   *Treaty on the Non-Proliferation of Nuclear Weapons*. International Atomic Energy Agency INFCIRC/140, April 22, 1970.

[50]   Tsoulfanidis, N. *Measurement and Detection of Radiation*. Washington DC: Taylor & Francis, 1995.

[51]   Valentine, T. E. *MCNP-DSP Users Manual*. 2001.

[52]   Verbeke, J. M. et al. "Simulation of Neutron and Gamma Ray Emission from Fission and Photofission". *UCRL-AR-228518, Lawrence Livermore National Laboratory* (2014).

[53]   White, G. "Review of Prior U.S. Attribute Measurement Systems". *LLNL-CONF-563691, Lawrence Livermore National Laboratory* (2012).

[54]   Woolf, A. F. "The New START Treaty: Central Limits and Key Provisions". *Congressional Research Service* (2017).

[55]   Zarimpas, N. *Transparency in Nuclear Warheads and Materials: The Political and Technical Dimensions*. Oxford University Press, 2003, p. 276.

APPENDIX

APPENDIX

SIMULATION METHODOLOGY

Simulating a measurement involved the following seven steps:

1. Source creation and simulation.

2. Light output conversion and Gaussian smearing.

3. Conversion to absolute time and source combination.

4. Conversion of interaction position to pixel.

5. Correction for detector dead time.

6. Particle identification.

7. Estimation of apparent time-of-flight and excess time.

Steps 1 and 6 are described in Section 4.1, and step 7 is described in Section 3.2. The remainder of the steps are described here.

Light Output Conversion and Gaussian Smearing

MCNPX-PoliMi records energy deposition for each interaction in the user-defined cells of record. This energy was first converted to light output and then corrected for the light output resolution of the detectors.

The light output due to a recoil proton energy ΔE is

$$L(\Delta E) = 0.75\Delta E - 3.2[1 - \exp(-0.22\Delta E)], \tag{1}$$

as described in Section 2.4. The light output was then smeared to account for the light output resolution of the detectors by randomly sampling from a Gaussian distribution with mean L and standard deviation σ determined by

$$\sigma = \frac{\sqrt{0.27^2 L^2 + 0.084^2 L + 0.053^2}}{2.35}. \tag{2}$$

The coefficients in both Equation 1 and Equation 2 are experimentally determined constants for EJ-299 scintillators published by Lawrence [24]. This process was conducted for each interaction in each cell. The total light output for a series of interactions was accumulated as a single interaction because the combined duration of the interactions is less than the charge collection time of the photomultiplier tube.

Conversion to Absolute Time and Source Combination

MCNPX-PoliMi records the time of interaction in user-specified cells relative to the start of each history. The fission simulations therefore record time of interaction from the original spontaneous

90

fission, while decay gamma simulations record time from the decay. In order to replicate the time behavior of events measured by the NCAI, the start time of each history was uniformly distributed over the duration of the actual real time. A uniform distribution was chosen because each history (spontaneous fission or decay) is independent of every other history.

Conversion of Interaction Position to Pixel

MCNPX-PoliMi records the interaction position in each user-specified detector cell. In terms of the model geometry, the (y) horizontal and (z) vertical distance from the detector assembly center provides the position in the imaging plane. These coordinates were mapped to pixels (0 to 1599), providing the basis of forming the encoded picture $P(k, l)$ in terms of the NCAI variables.

Correction for Detector Dead Time

An examination of the time between events in the same detector block for the DAF measurements showed a dead time of $2.15 \mu s$. This dead time was incorporated into the simulation by rejecting events in the same block within a $2.15 \mu s$ interval.